ANEUMOBENCH: A SOURCE-LINKED BENCHMARK FOR SYNTHETIC-GEOMETRY TRANSFER IN ANEURYSM CFD

Xigui Li[1,2] **Yuanye Zhou**[2] **Feiyang Xiao**[1,2] **Xin Guo**[1,2,†] **Chen Jiang**[1,2]
Tan Pan[1,2] **Xingmeng Zhang**[1,2] **Cenyu Liu**[2] **Zeyun Miao**[1,2] **Xiansheng Wang**[2]
Qimeng Wang[2] **Yichi Zhang**[1,2] **Wenbo Zhang**[1,2] **Hongwei Zhang**[1,2] **Ruoxi Jiang**[1,2]
Fengping Zhu[1,2] **Limei Han**[1,2] **Chensen Lin**[1,2,†] **Yuan Cheng**[1,2,†]

guoxin@sais.org.cn {lixigui, linchensen, cheng_yuan}@fudan.edu.cn

[1]Fudan University
[2]Shanghai Academy of Artificial Intelligence for Science

arXiv:2505.14717v2 [eess.IV] 30 Sep 2026

ABSTRACT

Scientific machine learning uses simulation data to train surrogate models for fast physical-field prediction across geometries. Local shape editing can expand limited geometry collections, but whether its variants improve prediction on unseen geometries, and how to allocate them across sources, require controlled evaluation. We introduce **AneumoBench**, a dataset and benchmark linking 401 source aneurysm geometries to 9,693 locally edited descendant records, with computational fluid dynamics (CFD) fields computed on both. It contains 80,752 steady velocity–pressure cases across eight inlet conditions and 9,715 transient sequences of velocity, pressure, and wall shear stress (WSS). Each sequence contains 100 frames sampled at 0.01-s intervals from a 1-s cardiac cycle. Mesh, point, and voxel interfaces support steady field prediction and WSS forecasting from four observed frames. With family-disjoint splits, we compare source-only training, descendant training, and descendant pretraining followed by source fine-tuning across nine architectures on 79 held-out sources. Under the reported schedules, two-stage training lowers steady-field and reset-window WSS errors relative to source-only training. With the number of sampled fields and training updates fixed within each comparison, GraphSAGE benefits from descendant training and from distributing a fixed number of descendants across more sources. For WSS, reset-window gains do not consistently persist through 96-step rollout, and lower trajectory error need not improve cycle-level shear metrics or hotspot localization. These data and protocols enable researchers to compare descendant selection and training strategies on the same unseen source geometries.

1 INTRODUCTION

Scientific machine learning aims to accelerate physical-field prediction across geometries. For surrogate models trained on simulation data, prediction on unseen geometries depends on model design and the range of geometries in the training set (Wu et al., 2024). The cost of preparing, meshing, and simulating geometries limits the amount of training data. Intracranial aneurysms provide a challenging setting: complex vessel and sac shapes affect the flow (Sforza et al., 2009; Xiang et al., 2011). Extending prediction beyond a limited source collection requires deciding which additional geometries to simulate.

Methods for learning physical fields include physics-informed neural networks (PINNs) (Raissi et al., 2019) and neural operators such as DeepONet and FNO (Lu et al., 2021; Li et al., 2021). Recent work has advanced geometry-aware prediction through both model design and larger computational fluid dynamics (CFD) datasets (Wu et al., 2024; Garnier et al., 2025). AirfRANS and DrivAerNet++ support evaluation across engineered geometries (Bonnet et al., 2022; Elrefaie et al.,

[†]Corresponding authors.

2024), while AneuG-Flow provides generated aneurysm geometries with steady and pulsatile fields (Ding et al., 2025). For local variants of a limited source collection, we ask whether their recomputed fields improve prediction on unseen sources and how a fixed number of variants should be distributed among sources.

Local shape editing creates related variants that share a source geometry's vessel context. We call these variants descendants; a source and its descendants form a source family. A pool of 280 descendant records can contain one variant from each of 280 sources or eight from each of 35. The total is the same, but the number of sources and the number of descendants per source differ. Comparing these choices requires CFD fields linked to each source and descendant, selectable training pools, and test sets that hold out entire source families. Within each comparison, we use the same number of sampled fields and training updates.

We introduce **AneumoBench**, a dataset and benchmark for studying the training value of locally edited aneurysm geometries (Figure 1). It links each descendant to its source, includes CFD fields on both, and provides mesh, point, and voxel interfaces. The reference tasks are steady velocity–pressure prediction and wall shear stress (WSS) forecasting from four observed frames.

Our contributions are:

- We construct **AneumoBench** with 401 source geometries and 9,693 locally edited descendant records, each linked to its source and inheriting its split. The corpus contains 80,752 steady cases across eight inlet conditions and 9,715 transient sequences. Each sequence records volume velocity and pressure and wall WSS over one 1-s cardiac cycle, with 100 frames sampled at 0.01-s intervals.
- We benchmark nine architectures on steady velocity–pressure prediction and WSS forecasting, using source-only, descendant-trained, and descendant-to-source recipes evaluated on 79 held-out source geometries. WSS evaluation includes four-step reset windows, 96-step rollouts, and cycle-level physical metrics.
- We use controlled GraphSAGE experiments to compare descendant pool sizes and allocations across sources. Training on descendant fields improves prediction, and distributing a fixed number of descendants across more sources lowers error; airfoil allocation rankings differ by model. We also test whether WSS transfer gains persist across forecast horizons and correspond to improvements in cycle-level shear metrics and hotspot localization.

2 Related Work

Scientific-ML datasets and benchmarks. Scientific-ML benchmarks evaluate variation across geometries and prediction through time. For geometry-based tasks, AirfRANS and DrivAerNet++ evaluate field prediction across engineered shapes (Bonnet et al., 2022; Elrefaie et al., 2024), while AFBench studies airfoil generation and editing (Liu et al., 2024).

For temporal prediction, PDEBench provides time-dependent partial differential equation (PDE) simulation tasks, and APEBench emphasizes autoregressive training and rollout (Takamoto et al., 2022; Koehler et al., 2024). BubbleML and LagrangeBench provide multiphase-flow and particle-based simulation tasks (Hassan et al., 2023; Toshev et al., 2023). RealPDEBench pairs numerical simulations with real-world measurements to evaluate simulation-to-measurement transfer (Hu et al., 2026). Table 1 compares the data relationships and evaluation settings of selected resources.

Aneurysm datasets. Aneurysm research includes detection and segmentation methods (Bo et al., 2021; Cao et al., 2025) and annotated imaging or geometry datasets (Timmins et al., 2021; Di Noto et al., 2023; Chen et al., 2024; Ivantsits et al., 2022; de Nys et al., 2024; Yang et al., 2020). Aneurisk and AneuX provide vascular surfaces and morphology records (Aneurisk-Team, 2012; Juchler et al., 2022), while CMHA adds hemodynamic annotations (Song et al., 2024). AneuG-Flow generates aneurysm sacs and parent vessels with steady and pulsatile CFD fields (Ding et al., 2025). BenchAnXplore combines patient-derived aneurysm bulges with idealized parent vessels for transient prediction (Lannelongue et al., 2026). AneumoBench links locally edited descendants to their source geometries and CFD fields for training-pool comparisons under family-disjoint evaluation.

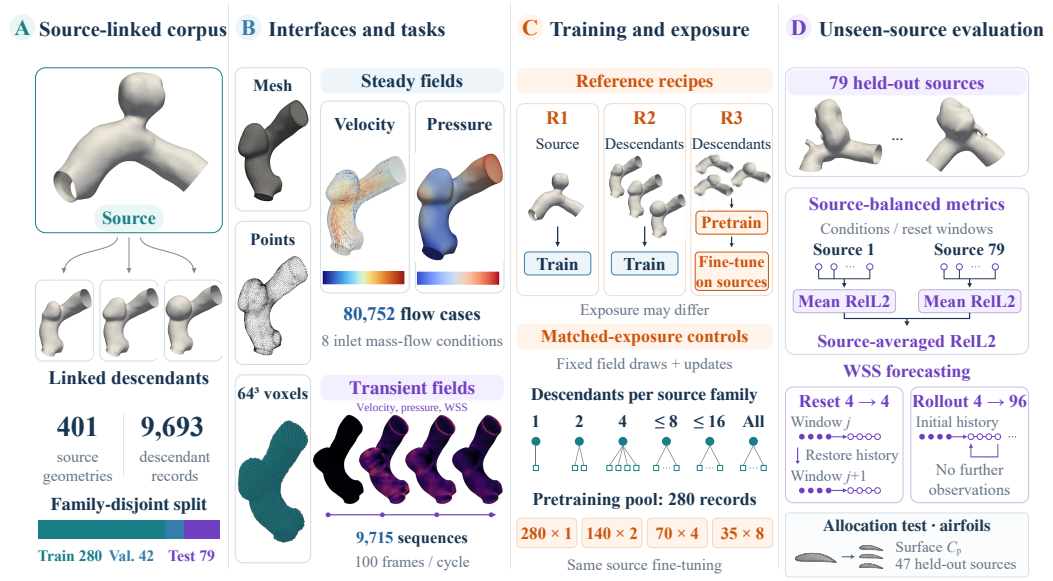


Figure 1: **AneumoBench corpus and benchmark.** **(A)** Family-disjoint splits contain 401 sources and 9,693 descendants (280/42/79 sources). **(B)** Steady cases provide velocity and pressure at eight inlet conditions; transient sequences provide 100 frames of velocity, pressure, and WSS. Mesh, point, and voxel interfaces are available. **(C)** R1/R2/R3 compare source, descendant, and descendant-to-source training; GraphSAGE controls fix sampling and update counts. **(D)** Source-balanced WSS evaluation uses $4 \to 4$ reset and $4 \to 96$ rollout; the airfoil extension uses 47 held-out sources.

Table 1: Data relationships and evaluation settings in selected scientific-ML resources. Appendix Table 9 details aneurysm-resource coverage and protocol records.

Resource	Data structure	Evaluation setting	Time dependence
AneuG-Flow	Generated aneurysm geometries	Geometry-to-field learning	Steady and pulsatile
AirfRANS	Airfoils and operating conditions	Data scarcity and extrapolation	Steady
APEBench	PDE trajectories	Training and rollout	Time-dependent
RealPDEBench	Simulation–measurement pairs	Simulation-to-measurement transfer	Time-dependent
AneumoBench	Source-linked geometry families	Unseen-source prediction and training-pool comparisons	Steady and pulsatile

CFD surrogate models. FNO predicts fields on regular grids, while Transolver targets general geometries (Li et al., 2021; Wu et al., 2024). MeshMask studies masked mesh-node pretraining, and GA-Field repeatedly injects geometry embeddings during aerodynamic field prediction (Garnier et al., 2025; Zheng et al., 2026).

3 AneumoBench Dataset

3.1 Source geometries and descendant construction

AneumoBench contains 401 source geometries retained from an archived AneuX snapshot (Juchler et al., 2022). Each describes an aneurysm and its adjoining vessel segments. We preserve these geometries and their CFD fields and prepare separate editing surfaces for descendant construction.

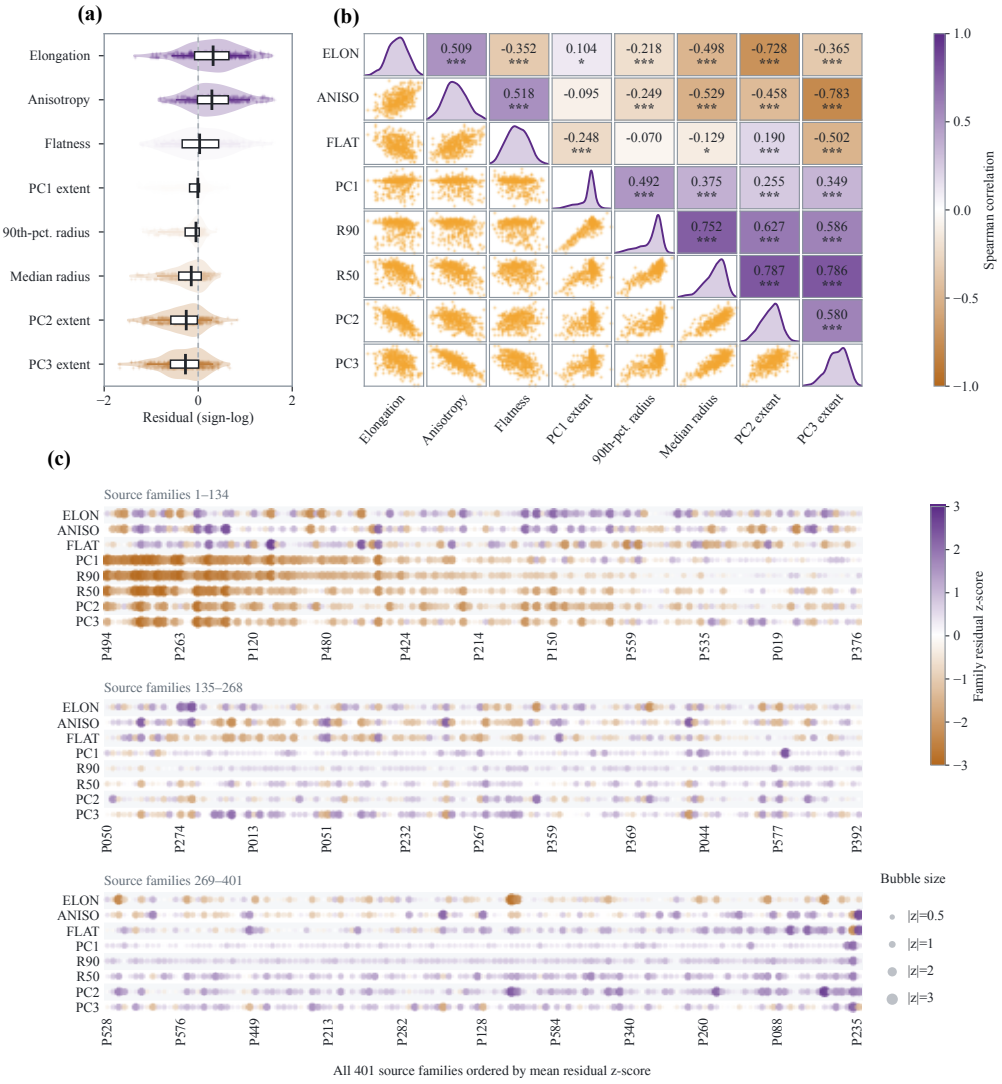


Figure 2: Geometry changes relative to each source. Each family contributes one median residual per descriptor. (a) Distributions of these residuals: positive values indicate larger descriptor values in descendants. Residuals use source-IQR scaling and a sign-log transform. (b) Spearman correlations of these family summaries; stars mark FDR-adjusted significance. (c) The residuals standardized across 401 families for each descriptor, showing departures from the mean family response. Color and bubble size encode signed and absolute z-scores. Families are ordered by mean z-score; Appendix A.5 gives the definitions.

To construct descendants, we inspect and repair the editing surface, remove the original aneurysm, and remesh the adjoining wall. A connected patch near the excision site is displaced by 0.5–1.0 mm along local normals and joined to the retained vessel through a transition band. We then smooth and remesh the surface before export. Patch selection and repair use operator-guided Geomagic Wrap operations. The resulting 9,693 descendant records retain source identifiers and CFD fields computed on each geometry. Appendix A.2 gives the construction details.

For 72.5% of descendants, the normalized distance to their source is below the median source–source distance. Across eight rotation-invariant descriptors, the median fraction of descendants within the sources' 5th–95th percentile ranges is 89.1%. The largest shifts are toward greater elongation and anisotropy (Figure 2). Appendix A.5 defines the surface distances and descriptors.

3.2 CFD DATA GENERATION

For each geometry, we designate the open end with the largest diameter as the inlet and the others as outlets. We impose zero-pressure outlet boundary conditions and no-slip vessel walls. Steady simulations use eight inlet mass-flow rates from 0.001 to $0.004\,\mathrm{kg\,s^{-1}}$ and store volume velocity and pressure. The resulting 80,752 cases each correspond to one geometry and one inlet condition.

Transient simulations run five cycles of a common 1-s inlet waveform. We retain 100 fifth-cycle frames at 0.01-s intervals for volume velocity and pressure and wall WSS. Before cohort filtering, the campaign used over 11 million CPU core-hours and produced approximately 23 TB of raw steady output and over 100 TB of raw transient output (Appendix B).

3.3 DATA ORGANIZATION AND VALIDATION

HDF5 records store fields, coordinates, connectivity, and boundary labels; transient records add timestamps and boundary-to-volume mappings for tracking wall locations (Appendix Table 12).

Reported steady results use arrays containing zero-valued placeholders at points unreferenced by cells. For new training, cell-connected preprocessing excludes these points from sampling, normalization, and voxel interpolation. Appendix H.4 defines this workflow and reevaluates six GraphSAGE allocation checkpoints on valid points with weights and normalization fixed.

Of 10,094 geometry records, 9,718 have converted transient HDF5 files; 376 descendants do not. Field and structural checks exclude three training-source sequences, leaving 9,715. Appendix B.5 documents finite-value, timestamp, and boundary-mapping checks and field-level conservation diagnostics.

3.4 DATA SPLITS

Sources are split into 280/42/79 training, validation, and test geometries, with descendants inheriting the assignment. The three transient exclusions leave 277 WSS training sources; validation and test sets remain unchanged. Appendix Table 6 gives cohort counts, and Appendix I specifies data access and review-package scope.

4 BENCHMARK DESIGN

4.1 PREDICTION TASKS

The **steady task** predicts velocity $\mathbf{u}$ and pressure p from geometry and inlet mass flow. Unstructured models receive coordinates, boundary type, wall distance, and flow rate at sampled volume points; voxel models receive occupancy, grid coordinates, and flow rate. Predictions are evaluated at sampled stored volume vertices or constructed fluid voxels, respectively.

The **WSS task** forecasts wall shear stress from geometry, four observed WSS frames, and the known target cardiac phase. Each history tracks a fixed wall location within a case. **Reset evaluation** predicts four frames autoregressively within each window and restores observed history at the next window. **Rollout evaluation** uses only the initial four observations to predict the remaining 96 frames autoregressively.

4.2 TRAINING DATA AND COMPARISON CONDITIONS

Source-only (R1) trains on source fields. **Descendant-trained (R2)** trains on descendants of the training sources. **Descendant→Source (R3)** starts from an R2 checkpoint and fine-tunes on source fields. Checkpoint selection uses source-validation data, and evaluation uses the same 79 test sources. For WSS, all three settings train with teacher forcing, appending an observed frame to the history at each step.

The **R1–R3 comparison** uses each setting's reported training schedule; the number of sampled fields and optimizer updates may differ. The **GraphSAGE controls** examine descendant pool size

and allocation, keeping these counts, normalization, and validation selection fixed within each comparison. The two controls use separate schedules (Section 5).

4.3 METRICS AND SOURCE-LEVEL STATISTICS

We compute relative ℓ_2 error (RelL2) for decoded velocity, pressure, and WSS, retaining the simulations' zero-pressure outlet reference. Errors are calculated per steady flow condition or reset window, then averaged within and across sources. For target $\mathbf{y}_{im}$ and prediction $\hat{\mathbf{y}}_{im}$ in case m of source i,

$$\mathcal{E}_{\mathrm{rel}} = \frac{1}{N}\sum_{i=1}^{N}\frac{1}{M_i}\sum_{m=1}^{M_i}\frac{\|\hat{\mathbf{y}}_{im}-\mathbf{y}_{im}\|_2}{\|\mathbf{y}_{im}\|_2+\epsilon_{\mathbf{y}}}, \tag{1}$$

where $N = 79$, and M_i is eight flow conditions or 19 stride-five reset windows. Thus each test geometry contributes equally. Rollout error compares all 96 predicted frames as one sequence per source.

Pressure diagnostics separate mean bias from error after removing the spatial mean. Time-averaged wall shear stress (TAWSS) is the cycle-average WSS magnitude at each wall location; oscillatory shear index (OSI) measures directional cancellation. We evaluate TAWSS and OSI field errors and overlap of the top-10% TAWSS locations. The predicted cycle contains four observations and 96 predictions. Appendix D defines these metrics and peak errors; Appendix C details spatial sampling.

Bootstrap intervals resample sources, describing test-source variation at one validation-selected checkpoint per architecture and setting in the R1–R3 comparison. Three-seed GraphSAGE controls and complete Transolver/U-Net WSS training runs assess training variability. The matched WSS experiment repeats only adaptation from fixed upstream checkpoints.

4.4 REFERENCE MODELS AND INPUTS

The unstructured models are PointNet, Transolver, and Galerkin Transformer on sampled points, and GraphSAGE on a 16-nearest-neighbor graph (Qi et al., 2017; Wu et al., 2024; Cao, 2021; Hamilton et al., 2017). The voxel models are U-Net, U-FNO, the Fourier neural operator (FNO), the U-shaped neural operator (U-NO), and the factorized Fourier neural operator (F-FNO) (Ronneberger et al., 2015; Wen et al., 2022; Li et al., 2021; Rahman et al., 2023; Tran et al., 2023). For WSS, voxel features are queried at wall points and combined with histories and phase. Both tracks use the same WSS wall queries. R1–R3 are compared within each architecture.

The main steady voxel results use unit-box coordinates, which omit absolute physical scale. U-Net and FNO reruns restore this scale with centered physical coordinates in metres (Appendix Table 31); this is the recommended coordinate input for new steady voxel experiments.

Persistence and linear extrapolation provide temporal predictions without training. We use history+phase ridge regression and PointwiseMLP to assess prediction from local histories and phase, without explicit coordinates or interactions between wall points. Appendices C and G.1 give implementation and training details.

5 BENCHMARK RESULTS

5.1 BASELINE RESULTS

Descendant pretraining followed by source fine-tuning lowers error across all nine architectures under the reported training schedules (Table 2). Relative to R1, R3 improves every primary endpoint, with median model-wise reductions of 18.8% for steady velocity, 13.5% for pressure, and 10.1% for reset-window WSS. Paired source-bootstrap confidence intervals (CIs) for the validation-selected checkpoints exclude zero for 8/9 velocity, 6/9 pressure, and 9/9 WSS architectures. Appendix E.3 reports the steady error distributions across sources.

Comparing R2 with R3, source fine-tuning further lowers velocity error for every architecture, while pressure error can increase or decrease. For GraphSAGE velocity, most of the reduction from R1 occurs during descendant training, with a smaller gain from fine-tuning.

Table 2: RelL2 for R1–R3 on 79 held-out sources under the reported training schedules. Each score uses one validation-selected checkpoint. Steady scores use sampled vertices from the original export arrays or the constructed fluid-voxel masks; Appendix H.4 separately reevaluates six GraphSAGE allocation checkpoints on cell-connected queries. Source-bootstrap intervals describe held-out-source variation. Lower is better; bold and underlined values mark the best and second-best recipes for each model–endpoint pair.

	Steady velocity			**Stored-gauge pressure**			**Reset-window WSS**		
Model	R1	R2	R3	R1	R2	R3	R1	R2	R3
Unstructured sampled points									
GraphSAGE	0.8269	0.6812	**0.6521**	0.7131	**0.5480**	0.5525	0.3571	0.2561	**0.2235**
Transolver	1.0031	0.7329	**0.6979**	0.8672	0.5808	**0.5783**	0.1253	0.1092	**0.1084**
Galerkin Transformer	1.0033	0.8477	**0.8150**	0.8682	**0.6417**	0.6667	0.1210	0.1094	**0.1090**
PointNet	0.9859	0.9371	**0.8899**	0.8489	0.7732	**0.7718**	0.1889	**0.1481**	0.1484
Regular voxel geometry (64^3, unit-box reference inputs)									
U-Net	0.9867	0.7916	**0.7050**	0.8147	0.7970	**0.7930**	0.2369	0.2216	**0.2064**
U-FNO	0.9859	0.8272	**0.7568**	0.9167	**0.7722**	0.7925	0.2442	0.2315	**0.2227**
FNO	1.0099	0.8592	**0.8387**	1.3334	1.0614	**0.9126**	0.2387	0.2243	**0.2145**
U-NO	0.9957	0.8829	**0.8303**	0.9490	0.8984	**0.8946**	0.2449	0.2320	**0.2230**
F-FNO	1.0153	1.0755	**1.0005**	1.3032	1.1677	**1.1466**	0.2334	0.2209	**0.2104**

Pressure results also depend on the metric and coordinate representation. After removing the spatial mean, R3 still lowers pressure RelL2 relative to R1 for GraphSAGE and Transolver (Appendix Table 30). For U-Net, R3 raises this error with unit-box inputs but lowers it with physical coordinates (Appendix Table 31).

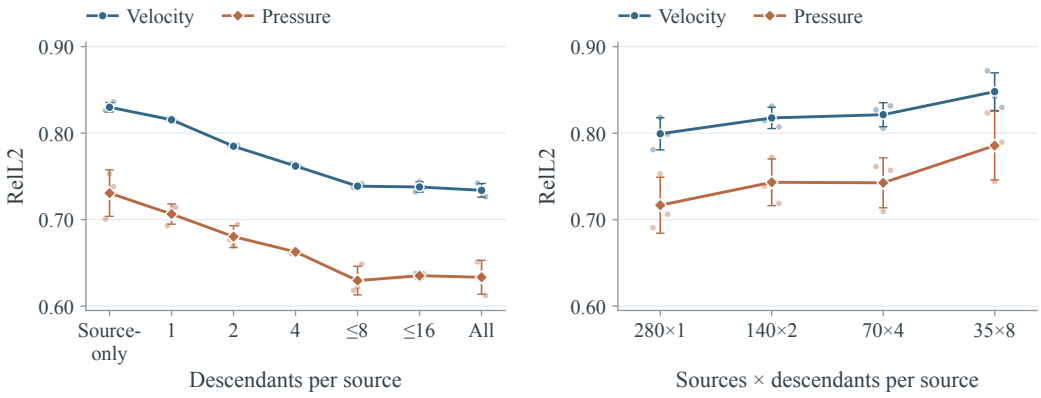
5.2 Number and allocation of descendants

To examine data selection, the GraphSAGE controls hold sampling and update counts fixed within each experiment. Increasing the descendant pool improves prediction, with gains that level off as the pool grows (Figure 3a). The pool-size control includes all 280 training sources and increases the accessible descendant count per source. Every run, including Source-only, samples 2,240 fields per epoch and performs 28,000 updates. Pool membership is fixed across seeds (Appendix Table 20).

A cap of eight descendants per source reduces velocity and pressure error by 11.0% and 13.8% relative to Source-only. Every tested pool improves both endpoints in all three seeds. Expanding beyond approximately eight descendants per source, up to the full pool, yields little additional improvement under this schedule.

At a fixed total of 280 descendants, broader source coverage gives GraphSAGE lower mean errors (Figure 3b). We compare 280 sources with one descendant each, 140 with two, 70 with four, and 35 with eight. Each allocation receives 28,000 descendant-training updates followed by 14,000 fine-tuning updates on the same fields from all 280 training sources, for a separate total budget of 42,000 updates.

Both endpoints have their lowest mean at 280×1. Concentrating the pool at 35×8 raises velocity and pressure errors by 6.1% and 9.6%, despite the shared source data used for fine-tuning. Reevaluation with fixed checkpoints and normalization also favors 280×1 on cell-connected queries, before and after removing orphan inputs (Appendix H.4).



(a) Pool expansion
28,000 updates

(b) Fixed-budget allocation
42,000 updates, including fine-tuning

Figure 3: GraphSAGE pool-size and allocation controls on 79 held-out sources. Small dots show individual seeds; connected markers and error bars give means and sample SD across seeds 42–44. Both panels use the same absolute RelL2 scale (lower is better); pressure uses the stored gauge. (a) Accessible-pool expansion. (b) Allocation of 280 descendants, followed by source fine-tuning. Within each panel, runs use equal numbers of sampled fields and training updates. Zero-velocity prediction has RelL2 approximately one. Complete values are in Appendix Tables 20 and 22.

Table 3: Airfoil pressure-coefficient RelL2 on 47 sources: mean ± sample SD across three full-pipeline seeds. The four 280-descendant allocations share a training budget; Source-only is a separately trained reference recipe. Bold marks the lowest mean within each model.

Model	Source-only	280×1	140×2	70×4	35×8
GraphSAGE	0.0482 ±0.0005	**0.0450 ±0.0001**	0.0463 ±0.0012	0.0453 ±0.0017	0.0454 ±0.0009
Transolver	0.0585 ±0.0115	0.0623 ±0.0028	0.0541 ±0.0129	0.0581 ±0.0089	**0.0516 ±0.0086**

5.3 Allocation on source-edited airfoils

To examine whether the allocation preference holds on another task and for another model, we train GraphSAGE and Transolver on source-edited AFBench airfoils (Liu et al., 2024). They predict recomputed surface pressure coefficients on a 256-point contour, using arc-length-weighted relative ℓ_2 error. Within each model, the four 280-record allocations share a two-stage schedule and are evaluated on 47 held-out sources across three full-pipeline seeds.

GraphSAGE has similar mean errors across allocations, with its lowest at 280×1; Transolver has its lowest at 35×8 (Table 3). For Transolver, changing from 280×1 to 35×8 lowers mean error by 17.2% and improves all three seeds. Compared with the separately trained Source-only reference, GraphSAGE at 280×1 also achieves lower error in every seed. Appendix F.3 gives construction and training details.

5.4 WSS forecasting across time horizons

For aneurysm WSS forecasting, short-window improvements do not consistently extend to uninterrupted rollout (Table 4). R3 lowers reset error relative to R1 for both Transolver and voxel U-Net across three independent training seeds. In rollout, Transolver improves in every seed, while U-Net has mixed seed-level changes and a $+0.2\%$ mean change. Transolver R3 has lower error than persistence over four steps but higher error over 96.

Table 4: Mean reset-window and recursive-rollout RelL2 across three training seeds.

Model	Reset window			96-step rollout			Pattern
	R1	R3	Δ	R1	R3	Δ	
Transolver	0.128	0.109	-14.9%	1.279	0.966	-24.5%	Both improve
Voxel U-Net	0.247	0.208	-15.6%	0.954	0.956	$+0.2\%$	Reset gain; rollout mixed
PointwiseMLP	0.146	–	–	0.735	–	–	Local-history reference
Persistence	0.258	–	–	0.881	–	–	Training-free

Lower is better; Δ is the R1-to-R3 change. PointwiseMLP uses three R1 training seeds; persistence is deterministic. Sample SD and seed-level results are in Appendix Tables 24, 25, and 26.

Table 5: WSS endpoints after identical eight-epoch $F = 16$ feedback adaptation of fixed Transolver R1/R3 checkpoints. Entries are means $\pm$ sample SD over three adaptation seeds on 79 sources. Lower is better. Appendix Table 28 reports all endpoints.

Endpoint	R1 initialization	R3 initialization
96-step rollout RelL2	0.46840 ± 0.01369	0.37076 ± 0.00390
TAWSS relative error	0.32239 ± 0.02310	0.21591 ± 0.00458
OSI absolute error	0.02747 ± 0.00025	0.02836 ± 0.00013

Standard WSS training uses observed histories, whereas evaluation feeds predictions back into the history. We therefore examine four-step scheduled sampling and longer full-feedback windows with detached predictions (Appendix G.4). For Transolver, longer windows yield lower rollout error after 30 epochs of adaptation from the same R3 checkpoint (Appendix Figure 15).

R3 retains its advantage under matched feedback adaptation. We adapt the seed-42 Transolver R1/R3 checkpoints for eight epochs with $F = 16$ predicted frames per window, repeating adaptation with three paired seeds while keeping the upstream checkpoints fixed. R3 has 20.8% lower mean rollout RelL2 (Table 5). Before adaptation, R3 outperforms R1 on 27 of 79 sources despite its lower mean error. After adaptation, R3 outperforms R1 on 72, 74, and 72 sources across the three seeds.

Lower rollout error does not ensure better cycle-level metrics or high-shear localization. In the standard pipelines, R3 lowers TAWSS error for Transolver but raises it for U-Net on average across seeds. After matched feedback adaptation, Transolver R3 has lower TAWSS error than R1 but slightly higher OSI error. PointwiseMLP also has lower rollout error than persistence, yet its top-10% TAWSS overlap falls from 0.847 to 0.519 (Appendix G).

6 Discussion and Conclusion

We introduced AneumoBench, linking source aneurysm geometries and their locally edited descendants to corresponding CFD fields. Its steady-field prediction and WSS forecasting tasks use source-family splits to compare how descendant data and training strategies affect prediction on unseen source geometries.

Under the reported training schedules, descendant pretraining followed by source fine-tuning lowers steady-field and reset-window WSS errors across all nine reference architectures. In the GraphSAGE controls, gains level off as the descendant pool grows; distributing a fixed number of descendants across more sources yields lower mean errors. The airfoil experiments give different allocation preferences for GraphSAGE and Transolver, showing that allocation strategies should be evaluated for each model.

In WSS forecasting, short-window gains do not consistently persist through uninterrupted rollout, and trajectory error alone does not fully describe the recovery of cycle-level shear or high-shear regions. Evaluation therefore needs to specify the observation schedule and forecast horizon and assess TAWSS, OSI, and hotspot overlap alongside trajectory error. AneumoBench provides common data and protocols for studying when training on descendant fields improves prediction on unseen geometries and which flow features benefit.

ARTIFICIAL INTELLIGENCE USE STATEMENT

We used generative AI tools to assist with language editing, translation, and relevant literature searches, and used tools such as Codex to run code following the authors' instructions. All AI-generated or AI-modified content was reviewed by the authors before inclusion in the manuscript. AI tools were not used to generate the synthetic geometries or CFD-derived targets. The authors take responsibility for the final text, claims, code, and artifacts.

ETHICS STATEMENT

AneumoBench uses public, deidentified source geometries. No new human data were collected, and no identifiable information was accessed. The AneuX source record specifies the Creative Commons Attribution-NonCommercial 4.0 (CC BY-NC 4.0) license together with attribution and article-citation requirements. The release preserves these notices for derived geometry files. CFD targets are generated under standardized research assumptions and are intended for machine-learning evaluation, not clinical decision making. The release includes cohort, availability, and exclusion records so that downstream users can assess the scope of the benchmark.

REPRODUCIBILITY STATEMENT

An anonymized code ZIP is provided as supplementary material. The Figshare review collection hosts the review data and pretrained checkpoints: a full-schema inspection subset, native-resolution WSS arrays for 277 training and 42 validation sources, and a fixed-test inference package. The training arrays support source-only WSS training and feedback adaptation. The inference package supplies all 79 fixed-sample test sources and eight Transolver checkpoints for reset and rollout evaluation. Source-level records reconstruct the reported statistics. The full multimodal corpus will be released after de-anonymization with permanent hosting and the required upstream notices. Appendix I details the reproduction tasks and data scope.

ACKNOWLEDGMENTS

This research was supported by the NovaInspire platform of Shanghai Academy of Artificial Intelligence for Science. The computations in this research were performed using the CFFF platform of Fudan University.

REFERENCES

Aneurisk-Team. AneuriskWeb project website. Web Site, 2012.

Zi-Hao Bo, Hui Qiao, Chong Tian, Yuchen Guo, Wuchao Li, Tiantian Liang, Dongxue Li, Dan Liao, Xianchun Zeng, Leilei Mei, Tianliang Shi, Bo Wu, Chao Huang, Lu Liu, Can Jin, Qiping Guo, Jun-Hai Yong, Feng Xu, Tijiang Zhang, Rongpin Wang, and Qionghai Dai. Toward human intervention-free clinical diagnosis of intracranial aneurysm via deep neural network. *Patterns*, 2 (2):100197, 2021. ISSN 2666-3899.

Florent Bonnet, Jocelyn Mazari, Paola Cinnella, and Patrick Gallinari. Airfrans: High fidelity computational fluid dynamics dataset for approximating reynolds-averaged navier–stokes solutions. In *Advances in Neural Information Processing Systems*, volume 35, pp. 23463–23478, 2022.

Shuhao Cao. Choose a transformer: Fourier or galerkin. In *Advances in Neural Information Processing Systems*, volume 34, pp. 24924–24940, 2021.

Wei Cao, Xin Chen, Jianping Lv, Liang Shao, and Weixin Si. Semi-supervised intracranial aneurysm segmentation via reliable weight selection. *The Visual Computer*, 41:5421–5433, 2025.

Huijun Chen, Xihai Zhao, Rui Li, Haokun Li, Haozhong Sun, Ziming Xu, Haining Wei, Yan Li, Jiaqi Dou, and Xueyan Li. Intracranial aneurysm and intracranial artery stenosis detection and segmentation challenge, April 2024. Challenge description.

Chloe M de Nys, Ee Shern Liang, Marita Prior, Maria A Woodruff, James I Novak, Ashley R Murphy, Zhiyong Li, Craig D Winter, and Mark C Allenby. Time-of-flight MRA of intracranial aneurysms with interval surveillance, clinical segmentation and annotations. *Scientific Data*, 11: 555, 2024.

Tommaso Di Noto, Guillaume Marie, Sebastien Tourbier, Yasser Aleman-Gomez, Oscar Esteban, Guillaume Saliou, Meritxell Bach Cuadra, Patric Hagmann, and Jonas Richiardi. Towards automated brain aneurysm detection in tof-mra: open data, weak labels, and anatomical knowledge. *Neuroinformatics*, 21(1):21–34, 2023.

Wenhao Ding, Yiying Sheng, Simão de Castro, Hwa Leo, and Choon Hwai Yap. Aneug-flow: A large-scale synthetic dataset of diverse intracranial aneurysm geometries and hemodynamics. In *Advances in Neural Information Processing Systems*, volume 38, Main Conference. Curran Associates, Inc., 2025.

Mohamed Elrefaie, Florin Morar, Angela Dai, and Faez Ahmed. Drivaernet++: A large-scale multimodal car dataset with computational fluid dynamics simulations and deep learning benchmarks. In *Advances in Neural Information Processing Systems*, volume 37, pp. 499–536. Curran Associates, Inc., 2024.

Hongyang Gao and Shuiwang Ji. Graph u-nets. In *Proceedings of the 36th International Conference on Machine Learning*, volume 97 of *Proceedings of Machine Learning Research*, pp. 2083–2092. PMLR, 09–15 Jun 2019.

Paul Garnier, Vincent Lannelongue, Jonathan Viquerat, and Elie Hachem. Meshmask: Physics-based simulations with masked graph neural networks. In *International Conference on Learning Representations*, volume 2025, pp. 63228–63244, 2025.

Will Hamilton, Zhitao Ying, and Jure Leskovec. Inductive representation learning on large graphs. In *Advances in Neural Information Processing Systems*, volume 30, 2017.

Sheikh Md Shakeel Hassan, Arthur Feeney, Akash Dhruv, Jihoon Kim, Youngjoon Suh, Jaiyoung Ryu, Yoonjin Won, and Aparna Chandramowlishwaran. Bubbleml: A multiphase multiphysics dataset and benchmarks for machine learning. In *Advances in Neural Information Processing Systems*, volume 36, pp. 418–449, 2023.

Peiyan Hu, Haodong Feng, Hongyuan Liu, Tongtong Yan, Wenhao Deng, Tianrun Gao, Rong Zheng, Haoren Zheng, Chenglei Yu, Chuanrui Wang, Kaiwen Li, Zhi-Ming Ma, Dezhi Zhou, Xingcai Lu, Dixia Fan, and Tailin Wu. Realpdebench: A benchmark for complex physical systems with real-world data. In *International Conference on Learning Representations*, volume 2026, pp. 107143–107188, 2026.

Matthias Ivantsits, Leonid Goubergrits, Jan-Martin Kuhnigk, Markus Huellebrand, Jan Bruening, Tabea Kossen, Boris Pfahringer, Jens Schaller, Andreas Spuler, Titus Kuehne, Yizhuan Jia, Xuesong Li, Suprosanna Shit, Bjoern Menze, Ziyu Su, Jun Ma, Ziwei Nie, Kartik Jain, Yanfei Liu, Yi Lin, and Anja Hennemuth. Detection and analysis of cerebral aneurysms based on x-ray rotational angiography - the cada 2020 challenge. *Medical Image Analysis*, 77:102333, 2022. ISSN 1361-8415.

Norman Juchler, Sabine Schilling, Philippe Bijlenga, Vartan Kurtcuoglu, and Sven Hirsch. Shape trumps size: image-based morphological analysis reveals that the 3d shape discriminates intracranial aneurysm disease status better than aneurysm size. *Frontiers in neurology*, 13:809391, 2022.

Felix Koehler, Simon Niedermayr, Rüdiger Westermann, and Nils Thuerey. Apebench: A benchmark for autoregressive neural emulators of pdes. In *Advances in Neural Information Processing Systems*, volume 37, pp. 120252–120310. Curran Associates, Inc., 2024.

Vincent Lannelongue, Paul Garnier, Pablo Jeken-Rico, Aurèle Goetz, Philippe Meliga, Yves Chau, and Elie Hachem. Physics constrained graph neural network for real time prediction of intracranial aneurysm hemodynamics. *npj Digital Medicine*, 9(1):212, 2026.

Zongyi Li, Nikola Borislavov Kovachki, Kamyar Azizzadenesheli, Burigede liu, Kaushik Bhattacharya, Andrew Stuart, and Anima Anandkumar. Fourier neural operator for parametric partial differential equations. In *International Conference on Learning Representations*, 2021.

Jian Liu, Jianyu Wu, Hairun Xie, Guoqing Zhang, Jing Wang, Wei Liu, Wanli Ouyang, Junjun Jiang, Xianming Liu, Shixiang Tang, and Miao Zhang. Afbench: A large-scale benchmark for airfoil design. In *Advances in Neural Information Processing Systems*, volume 37, pp. 82757–82780. Curran Associates, Inc., 2024.

Lu Lu, Pengzhan Jin, Guofei Pang, Zhongqiang Zhang, and George Em Karniadakis. Learning nonlinear operators via DeepONet based on the universal approximation theorem of operators. *Nature Machine Intelligence*, 3(3):218–229, 2021.

Alberto Marzo, Pankaj Singh, Ignacio Larrabide, Alessandro Radaelli, Stuart Coley, Matt Gwilliam, Iain D Wilkinson, Patricia Lawford, Philippe Reymond, Umang Patel, et al. Computational hemodynamics in cerebral aneurysms: the effects of modeled versus measured boundary conditions. *Annals of biomedical engineering*, 39(2):884–896, 2011.

Charles R. Qi, Hao Su, Kaichun Mo, and Leonidas J. Guibas. Pointnet: Deep learning on point sets for 3d classification and segmentation. In *Proceedings of the IEEE Conference on Computer Vision and Pattern Recognition (CVPR)*, July 2017.

Md Ashiqur Rahman, Zachary E Ross, and Kamyar Azizzadenesheli. U-NO: U-shaped neural operators. *Transactions on Machine Learning Research*, 2023. ISSN 2835-8856.

Maziar Raissi, Paris Perdikaris, and George E Karniadakis. Physics-informed neural networks: A deep learning framework for solving forward and inverse problems involving nonlinear partial differential equations. *Journal of Computational Physics*, 378:686–707, 2019.

Olaf Ronneberger, Philipp Fischer, and Thomas Brox. U-Net: Convolutional networks for biomedical image segmentation. In *Medical Image Computing and Computer-Assisted Intervention – MICCAI 2015*, volume 9351 of *Lecture Notes in Computer Science*, pp. 234–241. Springer, 2015.

Daniel M Sforza, Christopher M Putman, and Juan Raul Cebral. Hemodynamics of cerebral aneurysms. *Annual review of fluid mechanics*, 41(1):91–107, 2009.

Miao Song, Simin Wang, Qian Qian, Yuan Zhou, Yi Luo, and Xijun Gong. Intracranial aneurysm cta images and 3d models dataset with clinical morphological and hemodynamic data. *Scientific data*, 11:1213, 2024.

Makoto Takamoto, Timothy Praditia, Raphael Leiteritz, Daniel MacKinlay, Francesco Alesiani, Dirk Pflüger, and Mathias Niepert. Pdebench: An extensive benchmark for scientific machine learning. In *Advances in Neural Information Processing Systems*, volume 35, pp. 1596–1611, 2022.

Kimberley M. Timmins, Irene C. van der Schaaf, Edwin Bennink, Ynte M. Ruigrok, Xingle An, Michael Baumgartner, Pascal Bourdon, Riccardo De Feo, Tommaso Di Noto, Florian Dubost, Augusto Fava-Sanches, Xue Feng, Corentin Giroud, Inteneural Group, Minghui Hu, Paul F. Jaeger, Juhana Kaiponen, Michał Klimont, Yuexiang Li, Hongwei Li, Yi Lin, Timo Loehr, Jun Ma, Klaus H. Maier-Hein, Guillaume Marie, Bjoern Menze, Jonas Richiardi, Saifeddine Rjiba, Dhaval Shah, Suprosanna Shit, Jussi Tohka, Thierry Urruty, Urszula Walińska, Xiaoping Yang, Yunqiao Yang, Yin Yin, Birgitta K. Velthuis, and Hugo J. Kuijf. Comparing methods of detecting and segmenting unruptured intracranial aneurysms on tof-mras: The adam challenge. *NeuroImage*, 238:118216, 2021. ISSN 1053-8119.

Artur Toshev, Gianluca Galletti, Fabian Fritz, Stefan Adami, and Nikolaus Adams. Lagrangebench: A lagrangian fluid mechanics benchmarking suite. In *Advances in Neural Information Processing Systems*, volume 36, pp. 64857–64884. Curran Associates, Inc., 2023.

Alasdair Tran, Alexander Mathews, Lexing Xie, and Cheng Soon Ong. Factorized fourier neural operators. In *The Eleventh International Conference on Learning Representations*, 2023.

Kristian Valen-Sendstad, Marina Piccinelli, Resmi KrishnankuttyRema, and David A Steinman. Estimation of inlet flow rates for image-based aneurysm cfd models: where and how to begin? *Annals of biomedical engineering*, 43(6):1422–1431, 2015.

Prem Venugopal, Daniel Valentino, Holger Schmitt, J Pablo Villablanca, Fernando Vinuela, and Gary Duckwiler. Sensitivity of patient-specific numerical simulation of cerebal aneurysm hemodynamics to inflow boundary conditions. *Journal of neurosurgery*, 106(6):1051–1060, 2007.

Gege Wen, Zongyi Li, Kamyar Azizzadenesheli, Anima Anandkumar, and Sally M. Benson. U-fno—an enhanced fourier neural operator-based deep-learning model for multiphase flow. *Advances in Water Resources*, 163:104180, 2022.

Haixu Wu, Huakun Luo, Haowen Wang, Jianmin Wang, and Mingsheng Long. Transolver: A fast transformer solver for PDEs on general geometries. In *Proceedings of the 41st International Conference on Machine Learning*, volume 235 of *Proceedings of Machine Learning Research*, pp. 53681–53705. PMLR, 21–27 Jul 2024.

Jianping Xiang, Sabareesh K. Natarajan, Markus Tremmel, Ding Ma, J Mocco, L. Nelson Hopkins, Adnan H. Siddiqui, Elad I. Levy, and Hui Meng. Hemodynamic–morphologic discriminants for intracranial aneurysm rupture. *Stroke*, 42(1):144–152, 2011.

Xi Yang, Ding Xia, Taichi Kin, and Takeo Igarashi. Intra: 3d intracranial aneurysm dataset for deep learning. In *Proceedings of the IEEE/CVF Conference on Computer Vision and Pattern Recognition (CVPR)*, June 2020.

Zhenhua Zheng, Lu Zhang, Junhong Zou, Shitong Liu, Zhen Lei, Xiangyu Zhu, and Zhiyong Liu. GA-Field: Geometry-aware vehicle aerodynamic field prediction. *arXiv preprint arXiv:2602.20609*, 2026.

A Dataset Composition and Geometry Construction

Sections A–B describe the geometry records and CFD generation. Representations and training settings are in Section C, and metric definitions are in Section D. Extended reference, training-pool, and WSS results follow in Sections E–G. Section H contains representation and field diagnostics; Section I gives data access and reproduction instructions.

A.1 Source geometries

AneumoBench uses data from the AneuX morphology database, an open-access, multi-centric database combining data from three European projects: AneuX project, @neurIST project and Aneurisk (Juchler et al., 2022). The archived source surfaces describe aneurysms and adjoining vessel segments. Source geometries and their computed fields remain separate records when descendants are constructed. The acquisition inventory and retained cohort are distinguished in Section A.4.

A.2 Descendant construction

Each construction starts from a public, deidentified AneuX triangular surface. The mesh is inspected and repaired for non-manifold edges, self-intersections, spikes, tunnels, and holes. We prepare a separate editing surface by removing the original aneurysm and remeshing the adjoining wall. A connected patch at the excision site is then displaced by $d \in [0.5, 1.0]\,\mathrm{mm}$ along local normals. A polygon transition band joins the modified patch to the retained vessel before global remeshing and STL export. Patch selection and repair use operator-guided Geomagic Wrap 2024 operations. The final surfaces and their CFD fields form the benchmark records used for training, with each descendant linked to its source in the manifest.

A.3 Source relationships and inherited splits

We sort the 427 source identifiers in the acquisition inventory and shuffle them with Python's `random.Random(42)`. A 70/10/20 split, with training and validation counts rounded to the nearest integer, initially assigns 299/43/85 sources to training, validation, and testing. Applying the initial eight-flow steady and transient eligibility filters within these partitions removes 19/1/6 sources, leaving 280/42/79 without reshuffling. Descendants inherit their source's assignment and are retained only if that source passes the filters. Training pools use descendants of training sources; validation and testing use held-out source geometries. The scripts `data/build_patient_split.py` and `data/build_strict_split.py` specify the procedure.

A.4 Cohort accounting and modality availability

The release manifest records source geometries, eligible descendants, and the modalities available for each record. Every retained geometry has eight steady conditions. The transient archive contains 9,718 HDF5 sequences (401 source and 9,317 descendant); excluding three training-source sequences leaves 9,715 for the benchmark.

The cohort is formed in three stages: inventory the collected geometries, apply the cross-modal inclusion rule, then record which targets are readable. The acquisition inventory consists of the archived source surfaces because their record-level correspondence to the complete AneuX collection is unavailable. Table 7 lists the exclusions at each stage. Every raw descendant has a source mapping; field-level CFD checks are described in Section B.5.

Transient availability is assessed after the cohort is fixed. Missing source files or unreadable pressure arrays can prevent conversion, leaving WSS availability unknown for those records. The manifest records each failure and its reason. Transient availability is 96.27%, 94.88%, and 96.26% in the train, validation, and test splits, respectively.

Three source transient cases are structurally readable but contain divergent fields outside the intended fifth-cycle interval. All three belong to the training partition and are excluded from the transient protocol, leaving the validation and test cohorts unchanged. Their descendants retain the inherited split and remain eligible for pretraining when their own converted fields are available.

Table 6: Cohort ledger. "Eligible" records belong to the construction manifest and have a retained source; "available" records have a readable modality that passes structural validation. Counts refer to the unit named in each row; source geometries are counted in the first row. Parentheses give each split's share of the row total.

Release unit	Train	Validation	Test	Total	Evaluation treatment
Source geometries	280 (69.8%)	42 (10.5%)	79 (19.7%)	401	Split unit
Descendant records, eligible	6,687 (69.0%)	1,055 (10.9%)	1,951 (20.1%)	9,693	Inherit source split
Distinct wall-coordinate arrays	6,638	1,052	1,943	9,633	Coordinate-array equality
Descendant transient, available	6,438 (69.1%)	1,001 (10.7%)	1,878 (20.2%)	9,317	Readable 101-entry HDF5
Descendant transient, unavailable	249	54	73	376	Tracked in manifest; excluded from transient use
Source transient, archived/readable	280	42	79	401	Three train-only exclusions below
Source transient, protocol-included	277	42	79	398	Test denominator remains 79

Table 7: Release-cohort accounting for the archived 427-surface acquisition inventory. The archive lacks a record-level mapping to the complete 668-record AneuX collection. Counts in overlapping exclusion categories are unioned before subtraction.

Population	Operational transition	Removed	Retained
Source acquisition inventory	Locally archived source surfaces	–	427
Sources	< 100 transient outputs (25) or no complete eight-flow steady set (1)	26	401
Raw descendant inventory	All records; every record has a source mapping	–	10,660
Descendants	Incomplete transient index (330) or missing eight-flow steady set (7), overlap 2	335	10,325
Descendants	Otherwise complete but linked to one of the 26 excluded sources	632	9,693
Descendants	Missing conversion source files	26	9,667
Descendants	Required pressure array unreadable in multimodal conversion	350	9,317
Archived source HDF5	Structurally readable source records	–	401
Source transient protocol	Numerically unusable training-source records (143, 246, 441)	3	398

A.5 Geometric coverage and repetition

The geometric audit uses one stored wall point set per record. We compute eight descriptors from the complete point set, then draw a deterministic 512-point sample after principal component analysis (PCA) alignment for surface-distance comparisons. For 72.5% of descendants, the source–descendant distance is below the median random source–source distance, so the synthetic cohort forms predominantly local neighborhoods around its sources. For each descriptor, we compute the fraction of descendants within the 5th–95th percentile range of the 401-source distribution. The median of these eight fractions is 89.1%. The largest shifts are toward greater elongation and anisotropy.

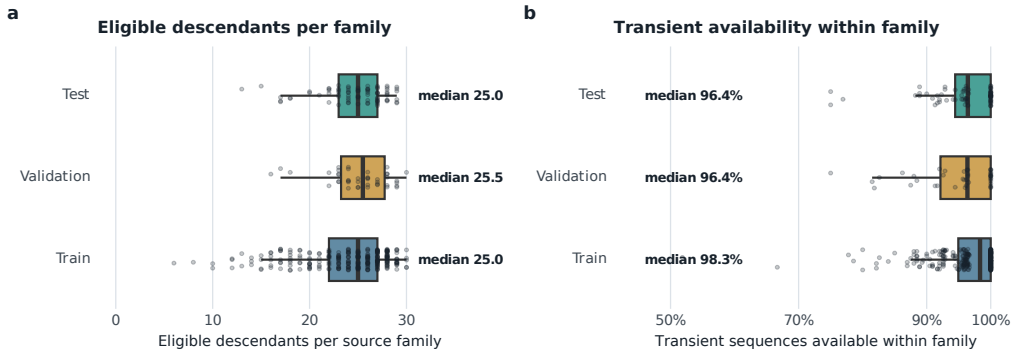


Figure 4: Descendant coverage for the 401-source/9,693-descendant manifest. (a) Eligible descendant counts and (b) transient availability within each lineage, grouped by inherited split. Each point represents a source lineage; boxes show the interquartile range and median, and labels give split medians. The manifest retains the source identifiers of the 376 unavailable descendant sequences.

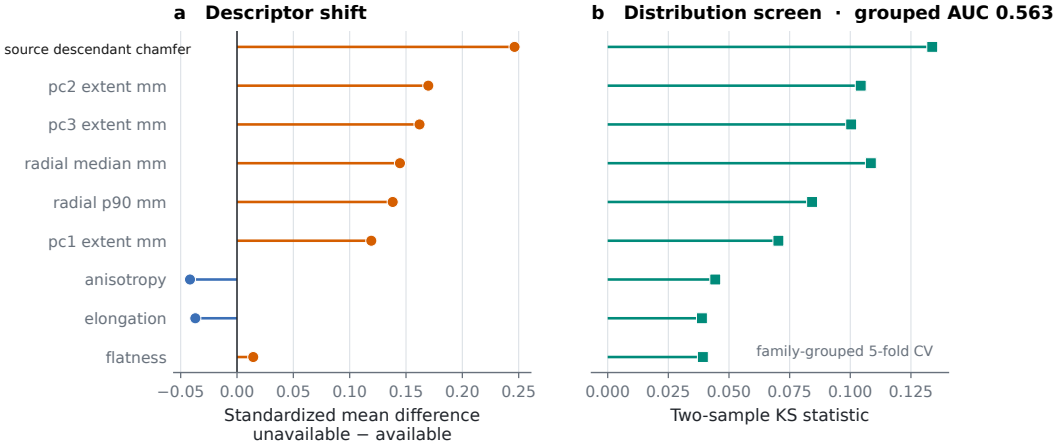


Figure 5: Geometry differences between the 376 descendants without a transient HDF5 file and the 9,317 available descendants. Standardized mean differences and Kolmogorov–Smirnov (KS) statistics compare eight rotation-invariant descriptors and source–descendant Chamfer distance. A class-balanced logistic model, evaluated by five-fold GroupKFold over lineages, achieves an out-of-fold area under the receiver operating characteristic curve (AUC) of 0.563. The recorded descriptors therefore predict availability only weakly.

Descriptor definitions. For wall coordinates $\mathbf{x}_a$ in metres, let $\bar{\mathbf{x}}$ be their arithmetic mean and $C = (n-1)^{-1}\sum_{a=1}^{n}(\mathbf{x}_a - \bar{\mathbf{x}})(\mathbf{x}_a - \bar{\mathbf{x}})^\top$ their covariance. Write its eigenvalues as $\lambda_1 \geq \lambda_2 \geq \lambda_3 \geq 0$, with unit eigenvectors $\mathbf{v}_k$. The three PC extents are $10^3[\max_a q_{ak} - \min_a q_{ak}]$ mm, where $q_{ak} = (\mathbf{x}_a - \bar{\mathbf{x}})^\top \mathbf{v}_k$. Median radius and 90th-percentile radius are the corresponding quantiles of $10^3\|\mathbf{x}_a - \bar{\mathbf{x}}\|_2$, also in mm. The remaining three descriptors are dimensionless:

$$\text{elongation} = \sqrt{\frac{\lambda_1 + \varepsilon}{\lambda_2 + \varepsilon}}, \qquad \text{flatness} = \sqrt{\frac{\lambda_2 + \varepsilon}{\lambda_3 + \varepsilon}}, \qquad \text{anisotropy} = \frac{\lambda_1 - \lambda_3}{\lambda_1 + \varepsilon}. \tag{2}$$

Here ε is double-precision machine epsilon, added to the numerical eigenvalues computed in square metres. These statistics weight stored wall vertices equally. Length descriptors retain physical scale; source-IQR normalization is applied only when comparing descriptor changes below. The implementation is `scripts/analyze_geometry_coverage.py`.

To compare the direction and size of descriptor changes across families, we scale each change by the spread among sources and summarize it within its family. For descendant j in the family D_i of source i and descriptor k, let IQR_k be the descriptor interquartile range across the 401 source geometries and define

$$\delta_{ijk} = \frac{x_{ijk}^{\text{descendant}} - x_{ik}^{\text{source}}}{\mathrm{IQR}_k}, \qquad r_{ik} = \mathrm{median}_{j \in D_i} \left[\mathrm{sign}(\delta_{ijk}) \log(1 + |\delta_{ijk}|) \right], \tag{3}$$

$$z_{ik} = \frac{r_{ik} - \bar{r}_k}{s_{r,k}}, \qquad \bar{r}_k = \frac{1}{401} \sum_i r_{ik}, \quad s_{r,k}^2 = \frac{1}{401} \sum_i (r_{ik} - \bar{r}_k)^2. \tag{4}$$

Figure 2(a,b) plots the lineage-median residuals r_{ik}. Panel (c) plots z_{ik}, with lineages ordered by their mean z-score across descriptors; zero corresponds to the mean residual across lineages. Color is clipped at ± 3, and bubble size saturates at $|z| = 3$. The script `scripts/plot_geometry_lineage_residuals.py` provides the figure data and transformations. Table 8 summarizes coverage, surface distances, and repeated geometries.

For PCA-canonical 512-point samples A and B, the normalized symmetric surface distance is

$$d_{\mathrm{sym}}(A, B) = \frac{1}{2s} \left[\frac{1}{|A|} \sum_{a \in A} \min_{b \in B} \|a - b\|_2 + \frac{1}{|B|} \sum_{b \in B} \min_{a \in A} \|b - a\|_2 \right], \tag{5}$$

where s is the mean of the two wall bounding-box diagonals. The distance compares the sampled shapes after PCA alignment.

Table 8: Geometric coverage and redundancy audit for the release cohort. Surface distances use 512-point deterministic samples after PCA canonicalization and are normalized by the mean wall bounding-box diagonal. Descriptor distances use median–IQR scaling fitted only on the 401 sources. Values are median [interquartile range]. Duplicate groups use coordinate-array equality; the near-neighbor rows report descriptor distances.

Audit quantity	Population / comparison	Result
Surface variation	Source–descendant ($n = 9,693$)	0.0519 [0.0421–0.0625]
Surface variation	Random source–source pairs ($n = 20,000$)	0.0613 [0.0533–0.0743]
Descriptor proximity	Nearest sibling	0.2056 [0.1481–0.2777]
Descriptor proximity	Nearest non-sibling	0.2614 [0.2045–0.3343]
Exact coordinate arrays	Groups / affected / excess records	47 / 107 / 60
Distinct coordinate arrays	One canonical record per exact group	9,633
Coverage	Descendants inside source 5–95% range	89.1% (median over descriptors)

Comparing stored coordinate arrays identifies 47 groups of identical arrays among 107 descendant records, leaving 9,633 distinct arrays (60 excess records; 0.62%). The reported total of 9,693 counts all eligible records, including the excess records. Each group belongs to one source lineage and split and is listed in the release manifest.

The fixed-budget allocation pools each contain 280 distinct stored wall-coordinate arrays for seeds 42–44. In the pool-size controls, $k = 1, 2, 4, 8, 16$ and full contain 0, 0, 2, 7, 24, and 49 excess records, respectively. These memberships are used for training.

A.6 Comparison with aneurysm resources

Table 9 compares resource size, CFD coverage, and the documented training and evaluation settings. BenchAnXplore combines patient-derived aneurysm bulges with idealized parent vessels in 105 geometries, with 80 frames per case (Lannelongue et al., 2026); our source-linked collection supports selecting multiple descendants per retained source.

Table 9: Comparison with aneurysm resources providing hemodynamic annotations.

Resource	Cohort size		CFD coverage		Benchmark protocol			
	Source units	Synthetic records	Steady	Pulsatile cases (frames)	Linked lineage	Inherited split	Matched exposure	Recursive rollout
Aneurisk	103	–	–	–	n/a	n/a	n/a	–
CMHA	143	–	–	–	n/a	n/a	n/a	–
AneuG-Flow	–	14,000	14,000	730 (80)	–	–	–	–
AneumoBench	**401**	**9,693**	**80,752**	**9,715 (100)**	**Yes**	**Yes**	**Yes**	**Yes**

Notes. Counts use the units reported by Aneurisk (Aneurisk-Team, 2012), CMHA (Song et al., 2024), and AneuG-Flow (Ding et al., 2025). Pulsatile entries give cases (frames); the AneumoBench count includes the 9,715 sequences used by the protocol. "Yes" indicates a documented property, "–" indicates that the cited paper and release documentation do not specify it, and "n/a" applies to protocols requiring a synthetic source–descendant cohort.

B CFD Generation and Field Quality

All velocity, pressure, and WSS targets are numerical CFD outputs. The term synthetic refers to geometry construction, described in Section A.2.

Generation scale. The simulation campaign used 24 processor cores per case and peaked at roughly 10,000 concurrent cores. Its records report approximately 23 terabytes (TB) of raw steady-state output and more than 100 TB of raw transient output, using over 11 million processor core-hours. These totals cover 85,280 steady cases and 10,660 transient cases before the cohort and modality filters in Section A. The retained representations are specified in Section C.

B.1 Domain, mesh, and boundary preparation

ANSYS 2026 R1 converts the repaired surface to a smooth boundary representation and meshes the vascular lumen as the fluid domain. Case-specific flow measurements are unavailable for this corpus, so we use standardized boundary conditions. Prior studies examine inflow estimation and the effects of modeled or measured boundary conditions in image-based aneurysm CFD (Valen-Sendstad et al., 2015; Marzo et al., 2011; Venugopal et al., 2007). During domain preparation, the open cross-section with the largest diameter is designated as the inlet and the remaining open ends as outlets. Each case stores the selected inlet and the complete boundary partition.

The CFD domains use unstructured polyhedral volume meshes with ten wall-adjacent inflation layers and layer growth rate 1.2. A single-case sensitivity study compared five global minimum sizes: 0.25, 0.20, 0.15, 0.10, and 0.05 mm. These settings produced roughly 0.15, 0.25, 0.33, 0.53, and 0.88 million cells, respectively. The velocity profiles change little between the 0.15- and 0.10-mm settings over the plotted interval (Figure 7a). This comparison informed the 0.15-mm production setting.

B.2 Steady solver and inlet conditions

The simulations solve the incompressible Newtonian Navier–Stokes equations with blood density $\rho = 1050\,\mathrm{kg\,m^{-3}}$ and kinematic viscosity $\nu = 3.2857 \times 10^{-6}\,\mathrm{m^2\,s^{-1}}$, corresponding to dynamic viscosity $\mu = 0.003449985\ \mathrm{Pa\,s}$. These values are fixed by the archived `transportProperties` dictionary for every case. Vessel walls are rigid and no-slip; outlets use zero relative pressure.

The steady suite uses eight inlet mass-flow rates: 0.001, 0.0015, 0.002, 0.0025, 0.003, 0.0035, 0.00375, and $0.004\,\mathrm{kg\,s^{-1}}$. Steady simulations use OpenFOAM v2312 `icoFoam` in pseudo-transient mode with the Pressure-Implicit with Splitting of Operators (PISO) algorithm for pressure–velocity coupling. The generation protocol requires velocity and pressure residuals below 10^{-5}.

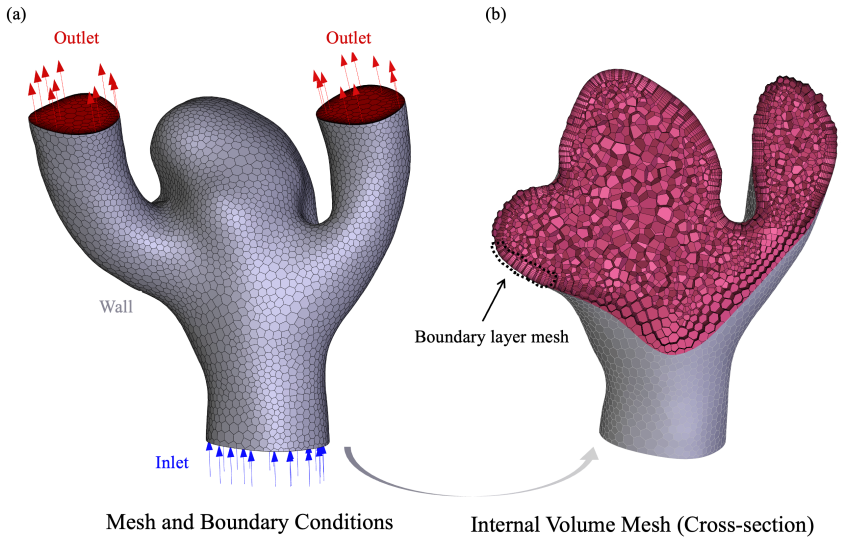
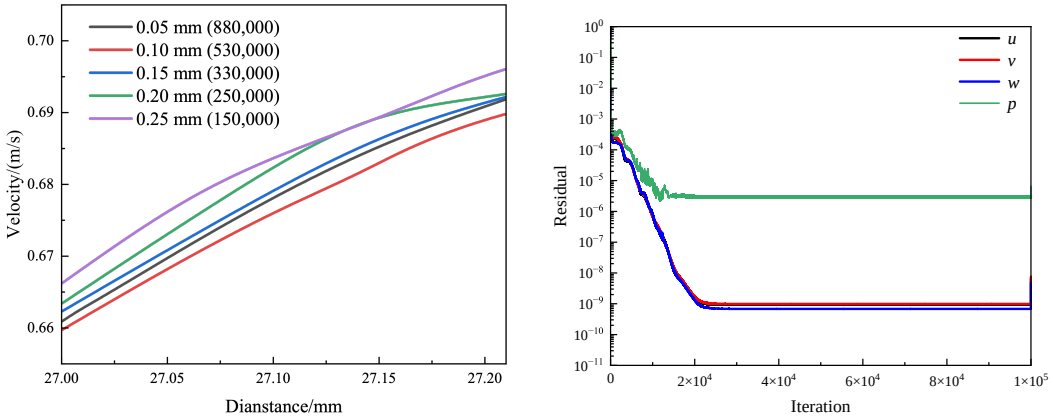


Figure 6: CFD domain construction. (a) Inlet, outlet, and wall boundaries on a representative surface mesh. (b) Cross-section of the internal volume mesh and its wall-adjacent boundary-layer cells.



(a) Velocity profiles across mesh resolutions.

(b) Steady-solver residuals.

Figure 7: Mesh-resolution comparison and steady-solver residuals. (a) Velocity profiles for one case at five mesh resolutions, used to inform the 0.15-mm production setting. (b) Velocity-component and pressure residuals over iterations for a representative steady case.

Representative completed runs typically reach velocity-component residuals below 10^{-9} and pressure residuals below 10^{-5}, consistent with Figure 7.

The project archive retains each case's runtime controls, numerical schemes, linear-solver settings, transport properties, and boundary-condition dictionaries. The steady corpus contains 77,544 descendant and 3,208 source flow-condition files.

B.3 Transient solver and retained cycle

For the transient suite, OpenFOAM v2312 `pimpleFoam` uses the common one-second pulsatile inlet waveform supplied with the release, a fixed 10^{-4}-s time step, and output every 100 steps. The 119-node inlet table uses `flowRateInletVelocity`, ranging from 1.50×10^{-6} to $1.45 \times 10^{-5}\,\mathrm{m^3\,s^{-1}}$ in the first cycle. Velocity is no-slip at walls and `inletOutlet` at outlets; pressure is zero-gradient at walls and the inlet and fixed to zero at outlets.

The PIMPLE algorithm, which combines PISO with the Semi-Implicit Method for Pressure-Linked Equations (SIMPLE), uses two pressure correctors, one non-orthogonal corrector, and up to 50 outer correctors. Pressure uses geometric agglomerated algebraic multigrid (GAMG; absolute tolerance 10^{-6}, relative tolerance 0.01), and velocity uses a symmetric Gauss–Seidel smoother (absolute tolerance 10^{-5}, relative tolerance 0.1).

The simulations use a fixed five-cycle duration, with four warm-up cycles and the fifth retained for analysis.

Each eligible transient HDF5 record contains the volume mesh, time-resolved velocity and pressure, boundary meshes and mappings, wall WSS vectors, and timestamps. One initialization entry precedes the 100 frames retained at 4.01–5.00 s. Field checks determine which converted records enter the benchmark (Section B.5); modality availability and conversion failures are recorded in Section A.4.

B.4 Equations and units

The simulations solve the incompressible Newtonian equations

$$\nabla \cdot \mathbf{u} = 0, \tag{6}$$

$$\frac{\partial \mathbf{u}}{\partial t} + (\mathbf{u} \cdot \nabla)\mathbf{u} = -\nabla p_k + \nu \nabla^2 \mathbf{u}, \tag{7}$$

where $p_k = p/\rho$ is kinematic pressure and $\nu = 3.2857 \times 10^{-6}\,\mathrm{m^2\,s^{-1}}$. With $\rho = 1050\,\mathrm{kg\,m^{-3}}$, the corresponding dynamic viscosity is $\mu = \rho\nu = 0.003449985\,\mathrm{Pa\,s}$. Rigid walls use a no-slip condition, and outlets use zero relative pressure. These assumptions are shared across all simulated geometries. The simulations omit wall compliance, non-Newtonian rheology, and case-specific outlet impedance.

OpenFOAM exports $\mathbf{u}$ in $\mathrm{m\,s^{-1}}$ and p_k in $\mathrm{m^2\,s^{-2}}$. The release converts pressure to Pa through $p = \rho p_k$. The stored `wallShearStress` vector is also in kinematic stress units; multiplying by ρ converts it to Pa. For a Newtonian fluid, the continuous tangential traction has the form

$$\boldsymbol{\tau}_w = \left(\mathbf{I} - \mathbf{n}\mathbf{n}^{\mathsf{T}}\right)\boldsymbol{\sigma}\mathbf{n}, \qquad \boldsymbol{\sigma} = -p\mathbf{I} + \mu\left(\nabla\mathbf{u} + \nabla\mathbf{u}^{\mathsf{T}}\right). \tag{8}$$

Here $\mathbf{n}$ is the unit wall normal directed out of the fluid domain and $\mathbf{I}$ is the identity tensor. The release preserves the OpenFOAM `wallShearStress` vector convention for $\boldsymbol{\tau}_w$. TAWSS and OSI are derived from this vector time series and remain invariant to a global sign reversal.

Table 10: Field and coordinate conventions used by the release and evaluator.

Quantity	Stored solver form	Released/evaluated form	Domain
Coordinates	Geometry source units standardized to metres	x, y, z in m; optional unit-bbox copy for intervention	Volume or wall vertices
Velocity	$\mathbf{u}$	$\mathrm{m\,s^{-1}}$	Internal volume mesh
Pressure	$p_k = p/\rho$	$p = \rho p_k$ in Pa	Internal volume mesh
Wall shear stress	Kinematic wallShearStress vector	$\boldsymbol{\tau}_w$ in Pa	Wall surface mesh
TAWSS	Not stored as a target	Cycle mean of $\|\boldsymbol{\tau}_w(t)\|_2$ in Pa	Wall surface vertices
OSI	Not stored as a target	Dimensionless vector-cycle index in $[0, 0.5]$	Wall surface vertices

B.5 Solver logs and field checks

The release connects each CFD target to its geometry, numerical configuration, and eligibility record. Machine-readable summaries report finite-value checks, field shapes, time grids, bound-

ary topology, and mass balance. Retained `pimpleFoam` logs document each source run; final-time directories match the sources admitted by the transient protocol.

Solver-log audit. A separate solver-log audit covers a fixed subset of 12 source geometries. All reached $t = 5$ after 50,000 steps, with an `End` marker and no fatal-error line. The median fraction of steps reporting PIMPLE convergence was 0.99998. In the fifth cycle, the fraction reaching the outer-iteration limit had median zero and maximum 0.0659. The maximum logged Courant number was 48.73. The largest absolute global continuity error over the audited runs was 3.57×10^{-5}.

Between cycles four and five, phase-aligned WSS component-extrema trajectories had a median relative ℓ_2 difference of 0.0302 (maximum 0.1776). Spatial fields are available only for the fifth cycle because `purgeWrite=100` removes earlier cycles. Selection and per-case records are in `data/validation/cfd_qc_selection_12real.json` and `data/validation/openfoam_solver_log_audit_12real.json`.

Full-field checks. Record validation covers all 9,718 converted transient HDF5 files available within the benchmark manifest: 401 sources and 9,317 descendants. Checks scan velocity, pressure, and WSS across all 101 stored entries and verify array shapes, timestamps, boundary mappings, and boundary polygon topology. Of these records, 9,715 pass. The three excluded source-training records (143, 246, and 441) have non-finite pressure values and invalid time grids; two also contain non-finite WSS values. Velocity is finite in all files. The per-record ledger and `data/validation/transient_field_audit_summary.json` report the checks and exclusions.

Field-level diagnostics summarize flow quantities and mass balance over every fifth non-initialization entry of the 9,715 retained records. Table 11 reports their distributions; range flags identify unusual values for inspection and are recorded separately from the field and structural checks.

The release metadata and the Reynolds and Womersley calculations use the transport parameters specified in Section B.4.

For the screening table, we use the equivalent inlet diameter $D = 2\sqrt{A/\pi}$ and framewise mean absolute normal inlet velocity $\bar{U}$. We compute $\mathrm{Re} = \bar{U}D/\nu$ and $\alpha = (D/2)\sqrt{2\pi/(T_c\nu)}$ with cardiac period $T_c = 1\,\mathrm{s}$.

Peak velocity is the largest internal-volume vertex magnitude over the 20 non-initialization frames retained by the stride-five audit. The 99th percentile of WSS magnitude (WSS p99) pools wall-vertex magnitudes over those frames. Relative residence time (RRT) is defined as $\mathrm{RRT} = 1/[(1 - 2\,\mathrm{OSI})\mathrm{TAWSS}]$. TAWSS, OSI, and RRT are first computed per wall vertex and then area-averaged; the RRT denominator is floored at 10^{-3} Pa.

Per-frame mass imbalance is $|\dot{m}_{\mathrm{in}} + \dot{m}_{\mathrm{out}}|/|\dot{m}_{\mathrm{in}}|$; the table reports its maximum, whereas the separate 6% screen applies to its cycle mean.

The Reynolds and Womersley empirical cumulative distribution functions (CDFs) are similar in Figure 8, indicating comparable inlet flow regimes under the shared boundary protocol. The wall responses differ: descendants have higher WSS p99 and mean TAWSS but lower median OSI and RRT. Synthetic pretraining therefore uses a related but shifted target distribution.

Screening intervals extend beyond the empirical tails of the source cohort and flag unusual records for inspection. Eligibility is determined by the field and structural checks. Overall, 98.03% of descendants receive no range flag; mean TAWSS and mean RRT account for the most frequent flags. Mass imbalance is assessed separately from these ranges and the full-field finite-value scan.

B.6 Ground-truth field diversity

The field galleries show how WSS, pressure, and speed vary spatially on individual source geometries. Sources are selected at approximately even intervals from the ordered test list.

Table 11: Transient CFD screening summaries. RRT denotes relative residence time. Values are median [interquartile range] across included records with a finite summary; n gives the case count for each diagnostic. Three divergent source sequences are excluded.

Diagnostic	Source geometries	n	Descendants	n
Mean Reynolds number	608 [479, 748]	398	602 [477, 743]	9,317
Womersley α	2.01 [1.63, 2.55]	398	2.03 [1.65, 2.56]	9,317
Peak velocity ($\mathrm{m\,s^{-1}}$)	3.53 [2.7, 5.02]	398	3.71 [2.75, 5.26]	9,317
WSS p99 (Pa)	146 [83.1, 249]	398	164 [93.4, 290]	9,317
Mean TAWSS (Pa)	17 [10.3, 27.8]	398	21.8 [13.2, 37.4]	9,317
Mean OSI	0.0224 [0.0144, 0.0356]	398	0.0182 [0.0125, 0.0274]	9,317
Mean RRT ($\mathrm{Pa^{-1}}$)	0.166 [0.0879, 0.287]	398	0.0992 [0.0594, 0.165]	9,317
Maximum mass imbalance	0.00246 [0.0011, 0.0063]	398	0.00441 [0.00149, 0.0115]	9,317
Records without any range flag	398 (100.00%)	398	9,133 (98.03%)	9,317

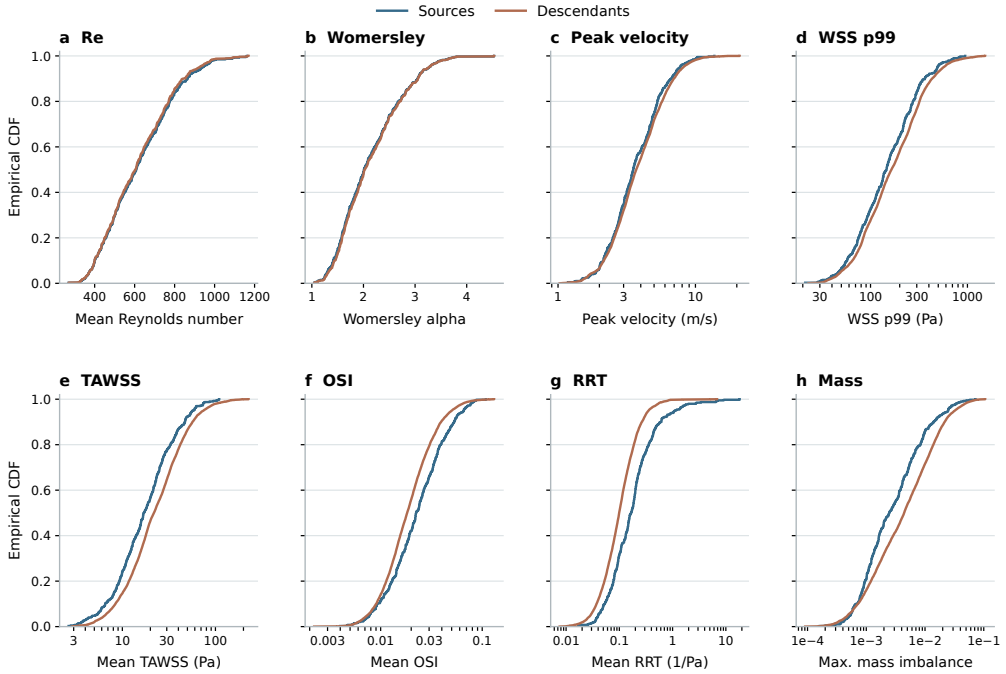


Figure 8: Empirical distributions for the audited transient cohort, including dimensionless flow descriptors, field magnitudes, and solver balance. The source curve contains 398 geometries and the descendant curve 9,317 available variants. Positive heavy-tailed quantities use logarithmic horizontal axes.

C Data Representations and Training Implementations

Sampling, coordinate transforms, and normalization convert the stored fields into model inputs. This section specifies those choices for each reference implementation.

C.1 Stored fields, schemas, and preprocessing

The dataset contains surface meshes (STL), voxel masks (`.nii.gz`), CFD meshes, mesh-resolved VTU/VTK exports, and ML-ready arrays. The mesh-resolved exports preserve the volume field



Figure 9: Ground-truth WSS for eight source geometries selected at approximately even intervals from the official test list, shown at four cardiac phases. All 32 panels use the released polygonal wall meshes and a shared color scale. Sources are arranged in two groups of four, with the same phase in corresponding rows. The gallery shows how the location and persistence of high-shear regions vary across source geometries.

(`internal.vtu`) and, when available, named inlet, outlet, and wall fields (`*.vtp`). These support physical-space inspection and alternative preprocessing. The temporal benchmark reads HDF5 records. Schemas document the arrays and units, while the manifest records split membership and availability.

For transient preprocessing, we drop the raw initialization frame, which has zero WSS, before forming prediction windows. Each protocol-included sequence then contains 100 valid cycle frames. The temporal models reported here are trained to predict WSS only.

C.2 Point sampling, graphs, and loader eligibility

The *unstructured* track supplies sampled points to point-set and attention models, or a 16-nearest-neighbor graph to GraphSAGE. The *voxel* track encodes geometry on a regular 64^3 grid. For transient WSS, it queries latent features at the same wall locations used by the unstructured track and

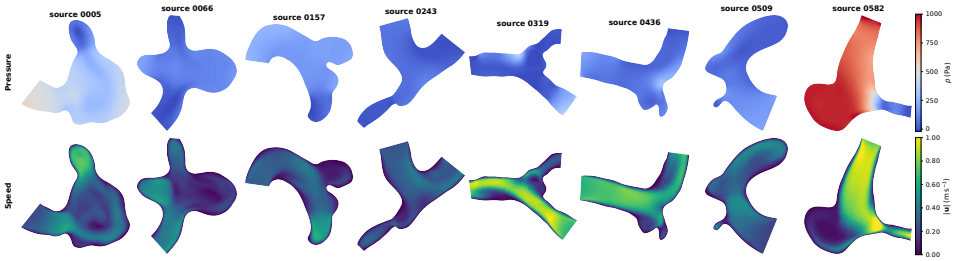


Figure 10: Ground-truth steady pressure and speed for eight approximately evenly spaced held-out source geometries at $0.003\,\mathrm{kg\,s^{-1}}$. Each column uses a deterministic geometry-centered PCA plane and the original VTU triangulation. Shared row colorbars show variation in the fields across geometries.

Table 12: Release representation schema. Counts distinguish geometries from flow-condition files and transient sequences.

Data form	Principal contents	Benchmark role	Audited accounting
STL surface	Vascular lumen boundary	Geometry/provenance	401 sources + 9,693 eligible descendant records
NIfTI mask	Binary voxelized lumen	Auxiliary binary geometry mask	Linked by geometry manifest
CFD mesh / VTU/VTK	Volume grid, boundary and field exports	Mesh-resolved CFD outputs and provenance	Availability recorded per modality
Steady HDF5	Coordinates, boundary/flow features, $\mathbf{u}$, p	Eight-flow field prediction	3,208 source + 77,544 descendant files
Transient HDF5	Volume mesh, $\mathbf{u}$, p, boundary meshes, WSS, time	WSS 4→4 and 4→96 forecasting; volume fields retained	401 archived source (398 usable) + 9,317 descendants

passes them to a pointwise history-and-phase decoder. Thus the geometry encoders differ, but the WSS output domain is shared.

Steady unstructured baselines sample 20,000 internal-volume vertices without replacement. Each sample includes physical coordinates, a four-way interior/wall/inlet/outlet code, wall distance, and an inlet-flow feature. Fixed diagnostics derive a stable seed from the case file and evaluate all vertices when a mesh has at most 20,000. Transient fixed evaluation uses seed $42+$case index and samples 4,096 wall vertices without replacement when possible; every test source exceeds this count.

Six training descendants have fewer than 4,096 wall vertices. The cached unstructured R2 loader excludes these 6 of 6,438 available cases (0.09%; 122,208 reset windows), whereas the case-grouped voxel R2 loader retains them by sampling with replacement (122,322 windows). This difference affects R2 training and, through the inherited R2 checkpoint, R3 initialization. Validation and test cohorts are identical across tracks.

C.3 Voxel construction, coordinates, and wall queries

For image-based protocols, 3D Slicer voxelizes the final surface into a binary Neuroimaging Informatics Technology Initiative (NIfTI) label map. The manifest links each mask to the corresponding geometry and CFD record.

The released NIfTI lumen mask differs from the 64^3 grid used by the baselines. For the baseline grid, internal volume-mesh vertices define a bounding box for each case. Coordinates are centered, divided by the longest bounding-box side, and translated to an endpoint-inclusive $[0, 1]^3$ lattice. Each grid location receives velocity and pressure from its nearest volume-mesh vertex. A voxel is

Table 13: Benchmark task card. The evaluation unit remains the source geometry even when a task contains multiple flow conditions, windows, frames, or points. Extended diagnostics include mean squared error (MSE), root mean squared error (RMSE), and mean absolute error (MAE).

Task	Data form	Model input	Target	Within-case sampling	Primary endpoint	Extended diagnostics
Steady field	Point / unstructured	xyz, boundary type, wall distance, mass flow	$\mathbf{u}, p$	20,000 sampled volume points; fixed diagnostic subset	Source RelL2	MSE, RMSE, MAE, R^2, direction
Steady field	Voxel 64^3	Occupancy, query coordinates, mass flow	$\mathbf{u}, p$	Complete constructed fluid mask	Source RelL2	Same physical-unit metrics
Transient reset	Point / surface	4 WSS frames, wall query, phase	Next 4 WSS frames	4,096 sampled wall points; fixed diagnostic subset; stride 5	Source-window RelL2	RMSE, magnitude and angle
Transient reset	Voxel 64^3	Occupancy grid, wall queries, 4 WSS frames, phase	Next 4 WSS frames	Same fixed wall subset	Source-window RelL2	Same physical-unit metrics
Transient rollout	Point or voxel	Geometry, phase, and first 4 WSS frames	Next 96 frames	No ground-truth reset	Mean E_i^{roll}	Mean cumulative error, TAWSS, OSI, top-10%, peak time/magnitude

marked as fluid when its normalized distance to that vertex is below $1.5/64$; targets outside this mask are zero. The models receive normalized coordinates, occupancy, and inlet flow. The stored bounding-box center and scale are omitted, so the input contains neither absolute physical size nor position.

Transient voxel models reuse the mask and transform of the $0.001\,\mathrm{kg\,s^{-1}}$ steady grid. Their latent features are queried at transformed wall points with trilinear `grid_sample`, border padding, and `align_corners=False`. All reported temporal voxel checkpoints use this decoder convention. Under the PyTorch sampling geometry, the endpoint-inclusive coordinates differ from endpoint-aligned interpolation by up to half a voxel. An alternative endpoint-aligned query transform is $g = (2u - 1)(R - 1)/R$ for normalized coordinate u and grid resolution R; checkpoint metadata record the sampling convention. Steady voxel endpoints are evaluated directly on the regular grid.

The steady coordinate-scale sensitivity retains the same occupancy grid but replaces each unit-box query coordinate $\mathbf{x}$ with $(\mathbf{x} - 0.5)s$, where s is the stored longest-side bounding-box scale. This transform restores centered physical coordinates while keeping the bounding-box center at the origin. It is evaluated for U-Net and FNO only; the core matrix and transient voxel track retain unit-box coordinates.

C.4 Normalization and domain shift

Each run estimates normalization statistics from its training data. In the core recipes, R1 and the fine-tuning stage of R3 use source-training statistics, whereas R2 uses descendant statistics. The GraphSAGE controls use the same source-training statistics in every branch. For WSS, statistics estimated from source-training windows are reused throughout R3 fine-tuning and evaluation. Predictions are decoded to SI units before auxiliary evaluation on held-out sources. The statistics in Table 15 also describe the descendant-to-source shift.

Table 14: Stage-wise provenance for the released representations. Source and geometry identifiers are preserved across every stage.

Stage	Input	Output	Recorded checks
Surface repair	Public-source triangular surface	Watertight repaired source surface	Topology defects, source identifier
Local deformation	Editing surface after sac removal and selected wall patch	Synthetic descendant surface	Source–descendant mapping and fixed output surface
Voxelization	Descendant or source STL	Binary NIfTI lumen mask	Geometry identifier, foreground/background convention
CFD preparation	Repaired STL	Named volume mesh and boundary patches	ANSYS 2026 R1; inlet/outlet/wall labels and mesh settings
Steady solve	Mesh and one mass-flow condition	$\mathbf{u}, p$ volume fields	OpenFOAM v2312 `icoFoam`; PISO; residual criterion and complete case configuration archived
Transient solve	Mesh and periodic waveform	101-entry raw field sequence	OpenFOAM v2312 `pimpleFoam`; $\Delta t = 10^{-4}$ s; PIMPLE/convergence logs and complete case configuration archived
ML packaging	Solver fields and geometry	HDF5, sampled point, and 64^3 representations	Units, shapes, split

Component means are small relative to their standard deviations because vessel orientation varies across cases. Synthetic velocity and WSS have consistently larger standard deviations. The pressure means are similar, but the synthetic standard deviation is 14% larger. The normalization sensitivity experiment holds architecture and training data fixed while changing the normalization statistics.

C.5 Reference architectures

The reference suite uses unstructured point sets, explicit k-nearest-neighbor (kNN) graphs, and regular voxel grids. Its models use message passing, attention, convolution, or spectral mixing.

C.6 Training recipes and checkpoint selection

R1 and R2 use the training sources and their descendants, respectively. R2 checkpoints are selected on source-validation data before R3 fine-tunes them on the source-training fields. The steady R1 corpus contains 2,240 fields per epoch; R2 contains 53,496. R1–R3 therefore differ in the number of sampled fields and training updates, initialization, and data composition.

All core runs use AdamW with weight decay 10^{-5}, a OneCycle schedule with warm-up fraction 0.3, zero dropout, and default seed 42. Table 18 gives the epoch counts and learning rates for R1–R3.

Steady training minimizes a single per-example RelL2 over velocity and pressure outputs concatenated after per-channel normalization. Core unstructured checkpoints are selected by validation velocity RelL2, while core voxel checkpoints use masked validation velocity RelL2. The GraphSAGE pool-size and fixed-budget allocation controls select on the mean of validation velocity and pressure RelL2. GraphSAGE uses batch size 32 in the core matrix and batch size 16 in its matched controls. Test endpoints are decoded to physical units and are not used for checkpoint selection.

Core transient R1/R2/R3 training appends observed WSS frames to the history at each step. Evaluation feeds back predictions, with observed histories restored between reset windows but not during the 96-step rollout. Section G examines training with prediction feedback over longer horizons.

Table 15: Output normalization statistics in channel order: u_x, u_y, u_z, p for the steady task and the three WSS components for the transient task. Velocity is measured in $\mathrm{m\,s^{-1}}$; pressure and WSS are in Pa.

Channel	Mean	Standard deviation
Steady source		
2,240 training flow cases; 514,573,832 points		
u_x	0.00069	0.17669
u_y	0.01249	0.16057
u_z	0.01157	0.17094
p	169.49	266.63
Steady descendant		
53,496 training flow cases; 9,962,079,176 points		
u_x	0.00007	0.20798
u_y	0.01719	0.18774
u_z	0.01553	0.19895
p	166.46	303.96
Transient source		
Window-weighted $H{=}4 \rightarrow F{=}4$ training frames		
τ_x	-0.2056	38.1109
τ_y	-1.1351	35.3612
τ_z	-1.6628	38.3904
Transient descendant		
Window-weighted $H{=}4 \rightarrow F{=}4$ training frames		
τ_x	-0.3560	45.6614
τ_y	-1.6134	42.8244
τ_z	-1.9307	45.7977

Table 16: Trainable parameter counts for completed R3 runs in each task, as recorded in the training logs. M denotes millions.

Model	Steady	Transient
Unstructured sampled points		
GraphSAGE	0.37M	0.37M
Transolver	3.86M	3.87M
Galerkin Transformer	1.10M	1.10M
PointNet	0.23M	0.23M
Regular voxel geometry (64^3)		
U-Net	51.89M	51.92M
U-FNO	217.06M	217.09M
FNO	113.28M	113.30M
U-NO	518.65M	518.68M
F-FNO	1.19M	1.22M

Checkpoint selection in the core unstructured steady and transient runs resampled point subsets on each validation pass; steady voxel validation used the complete regular grid. All extended diagnostics use fixed case-indexed subsets. Steady unstructured metrics are defined on internal volume-mesh vertices, steady voxel metrics on the constructed fluid mask, and both transient tracks on the same wall-query domain. Primary metrics use uniform vertex or mask weighting. Appendix Section H reports quadrature-weighted diagnostics.

Pool-size and allocation controls use the specific schedules and pool memberships in Section F. Additional temporal baselines and feedback-training settings are defined with their comparisons in Section G.

Table 17: Architecture and batch configurations. PointwiseMLP is an auxiliary transient diagnostic; the remaining rows form the nine-architecture reference suite. Width and depth follow the released implementations.

Model	Width	Depth	Heads	Batch (steady / transient)	Geometry/operator setting
PointwiseMLP (aux.)	128	4	–	– / 32	Shared residual multilayer perceptron; no point interaction
PointNet	16	8	–	32 / 64	Point-set multilayer perceptron
GraphSAGE	128	8	–	32 / 32	16-nearest-neighbor graph
Transolver	256	8	8	16 / 16	32 physics-attention slices
Galerkin Transformer	128	8	8	16 / 32	Galerkin attention
U-Net	64	4	–	32 / 16	64^3 voxel grid
U-FNO	64	4	–	16 / 16	12 Fourier modes
FNO	64	4	–	32 / 16	12 Fourier modes
U-NO	64	4	–	16 / 8	12 Fourier modes
F-FNO	64	4	–	32 / 16	12 factorized modes

Excluded implementation. The archived adapter for Graph U-Net (Gao & Ji, 2019) passed feature channels as spatial coordinates to its pooling and interpolation layers. Its steady and transient results are therefore excluded from the reference comparisons and cross-model summaries; the archived records retain their original identifiers.

Table 18: Optimization schedules for the core R1–R3 comparison. Table 17 lists batch sizes, widths, and key operator settings; the released configurations and logs give the full settings.

Regime	Training data	Initial weights	Steady epochs	Transient epochs	Learning rate	Selection / evaluation
R1	Source geometries	Random	200	200	10^{-3}	Minimum validation endpoint; held-out sources
R2	Synthetic descendants of training sources	Random	200	50	10^{-3}	Source-validation selection; common source test
R3	Source training geometries	Best R2 checkpoint	100	100	10^{-4}	Minimum validation endpoint; same test cohort

D Evaluation Metrics and Statistical Methods

Metrics are computed from decoded physical fields. The definitions below distinguish field errors, recursive prediction, pressure diagnostics, and cycle-level WSS quantities before specifying source-level aggregation.

D.1 FIELD AND DIRECTIONAL ERRORS

For a decoded steady field or reset window m from held-out source geometry i, let $j = 1, \ldots, J_{im}$ index the evaluated scalar entries, counting vector components separately. The metrics are

$$\mathrm{MSE}_{im} = J_{im}^{-1} \sum_j (\hat{y}_{imj} - y_{imj})^2, \qquad \mathrm{RMSE}_{im} = \sqrt{\mathrm{MSE}_{im}}, \tag{9}$$

$$\mathrm{MAE}_{im} = J_{im}^{-1} \sum_j |\hat{y}_{imj} - y_{imj}|, \qquad e_{im} = \frac{\|\hat{\mathbf{y}}_{im} - \mathbf{y}_{im}\|_2}{\|\mathbf{y}_{im}\|_2 + \epsilon_{\mathbf{y}}}, \tag{10}$$

$$R^2_{im} = 1 - \frac{\sum_j (\hat{y}_{imj} - y_{imj})^2}{\sum_j (y_{imj} - \bar{y}_{im})^2 + \eta_{R^2}}, \qquad \bar{y}_{im} = J_{im}^{-1} \sum_j y_{imj}. \tag{11}$$

Norm denominators use $\epsilon_z = 10^{-8}$ in the physical units of field z. The R^2 variance denominator adds $\eta_{R^2} = 10^{-8}$ in squared field units. Primary norms and means assign equal weight to the deterministically sampled entries; Appendix H reports the corresponding quadrature-weighted sensitivity analysis.

For a vector entry ℓ, directional metrics retain only

$$\mathcal{D}_{im} = \{\ell : \|\hat{\mathbf{y}}_{im\ell}\|_2 > 10^{-8} \ \wedge \ \|\mathbf{y}_{im\ell}\|_2 > 10^{-8}\}. \tag{12}$$

Cosine similarity averages the normalized dot product over $\mathcal{D}_{im}$. Angular error averages the arccosine of the clipped cosine similarities, converted to degrees. All thresholds and errors are applied after decoding to physical units; numerical denominator guards use the metric-specific constants above.

D.2 RESET-WINDOW, ROLLOUT, AND CUMULATIVE ERRORS

For a 4→4 reset window, the model receives four ground-truth WSS frames and predicts four future frames autoregressively. A 4→96 rollout uses the first four valid-cycle frames as observations, together with geometry and phase, and feeds predictions back for the remaining 96 steps. Let $\hat{\mathbf{W}}_{i,s}$ and $\mathbf{W}_{i,s}$ denote the predicted and target wall vectors, flattened over sampled vertices and components, for source i at step s. The primary source-level rollout error is

$$E_i^{\mathrm{roll}} = \frac{\left(\sum_{s=1}^{96} \|\hat{\mathbf{W}}_{i,s} - \mathbf{W}_{i,s}\|_2^2\right)^{1/2}}{\left(\sum_{s=1}^{96} \|\mathbf{W}_{i,s}\|_2^2\right)^{1/2} + \epsilon_{\mathbf{W}}}. \tag{13}$$

Its mean over the 79 sources is reported as rollout RelL2. Error accumulation is summarized by

$$C_i(s) = \left(\frac{\sum_{r=1}^{s} \|\hat{\mathbf{W}}_{i,r} - \mathbf{W}_{i,r}\|_2^2}{\sum_{r=1}^{s} \|\mathbf{W}_{i,r}\|_2^2 + \eta_C}\right)^{1/2}, \qquad \overline{C}_i = \frac{1}{96} \sum_{s=1}^{96} C_i(s). \tag{14}$$

The cumulative evaluator uses $\eta_C = 10^{-8}\,\mathrm{Pa}^2$ in its squared-energy denominator. Without numerical guards, $C_i(96)$ equals E_i^{roll}. The mean cumulative error $\overline{C}_i$ averages cumulative errors over forecast steps.

D.3 QUADRATURE, CENTERED PRESSURE, AND PRESSURE DROP

Quadrature and pressure-gauge sensitivity are evaluated separately from the primary, uniformly weighted evaluation. Let $k = 1, \ldots, K_{im}$ index spatial locations and let $q_{imk} \geq 0$ be normalized quadrature weights, $\sum_k q_{imk} = 1$. For steady unstructured fields, VTK computes cell volumes from the original `internal.vtu`. Each volume is divided equally among the cell's stored vertices, with contributions summed at shared vertices. All 79 held-out HDF5 geometries exactly match their source VTU point order, cell offsets, connectivity, and VTK cell types. Within each source, all eight steady conditions share that HDF5 mesh, and no nonpositive cell volume occurs.

Wall weights are obtained by fan-triangulating the native boundary polygons and lumping triangle area to their vertices.

Across the 79 source VTUs, 1,199,045 of 19,985,647 stored vertices (6.0%) are orphan points in the exported point arrays: they are not referenced by the volume-cell connectivity. Audited orphan entries store zero velocity and pressure, including positions inside active fluid cells; these are export placeholders rather than valid CFD point supervision. They remain in the uniform vertex-sampled endpoint and receive zero weight in the native-volume diagnostic. Volume weighting consequently removes the contribution of orphan points as well as changing the integration weights. Uniform voxel volumes cancel after normalization.

In the weighted error, $\mathbf{y}_{imk}$ collects the components at location k, including all four predicted frames for a reset window. The squared-energy guard is $\eta_q = 10^{-12}$ in squared field units for both quadrature-weighted and centered-pressure errors:

$$e_{im}^{(q)} = \left(\frac{\sum_k q_{imk} \|\hat{\mathbf{y}}_{imk} - \mathbf{y}_{imk}\|_2^2}{\sum_k q_{imk} \|\mathbf{y}_{imk}\|_2^2 + \eta_q} \right)^{1/2}. \tag{15}$$

Centered-pressure RelL2 subtracts each field's spatial mean to separate spatial mismatch from mean bias:

$$e_{im}^{\text{center}} = \left(\frac{\sum_k q_{imk} \{(\hat{p}_{imk} - \hat{\mu}_{im}) - (p_{imk} - \mu_{im})\}^2}{\sum_k q_{imk} (p_{imk} - \mu_{im})^2 + \eta_q} \right)^{1/2}, \tag{16}$$

$$\hat{\mu}_{im} = \sum_k q_{imk} \hat{p}_{imk}, \qquad \mu_{im} = \sum_k q_{imk} p_{imk}. \tag{17}$$

With $b_{im} = \hat{\mu}_{im} - \mu_{im}$ and $d_{imk} = (\hat{p}_{imk} - \hat{\mu}_{im}) - (p_{imk} - \mu_{im})$, the pressure error decomposes as

$$\sum_k q_{imk} (\hat{p}_{imk} - p_{imk})^2 = b_{im}^2 + \sum_k q_{imk} d_{imk}^2. \tag{18}$$

This decomposes stored-gauge squared pressure error into mean-bias and centered-field contributions under the same spatial weights. The analysis reports b_{im} separately, together with a sampled-edge pressure-gradient error and inlet–outlet pressure-drop error. The gradient diagnostic uses a fixed 16-nearest-neighbor graph as a local proxy. For pressure drop, $\mathcal{I}_{im}$ and $\mathcal{O}_{im}$ contain the evaluated vertices marked by the released inlet and outlet boundary codes. Cases with multiple outlets pool all outlet vertices. Using uniform means over the sampled vertices, the pressure-drop metric is

$$\Delta p_{im} = |\mathcal{I}_{im}|^{-1} \sum_{k \in \mathcal{I}_{im}} p_{imk} - |\mathcal{O}_{im}|^{-1} \sum_{k \in \mathcal{O}_{im}} p_{imk}, \qquad E_{im}^{\text{drop}} = \frac{|\widehat{\Delta p}_{im} - \Delta p_{im}|}{|\Delta p_{im}| + \epsilon_p}. \tag{19}$$

The absolute pressure-drop error is $|\widehat{\Delta p}_{im} - \Delta p_{im}|$ in Pa. Voxel inputs do not retain inlet and outlet query sets, so this diagnostic is reported only for the unstructured track.

D.4 Cycle-level WSS, hotspots, and peaks

TAWSS and OSI are evaluated over the retained fifth cycle. The predicted cycle combines four observed frames with 96 predictions; the target cycle uses all 100 CFD frames. Let $\mathbf{w}_{t,v}$ denote the WSS vector at wall vertex v and cycle frame t. For $N_t = 100$ equally spaced frames,

$$\text{TAWSS}(v) = \frac{1}{N_t} \sum_{t=1}^{N_t} \|\mathbf{w}_{t,v}\|_2, \tag{20}$$

$$\text{OSI}(v) = \frac{1}{2} \left(1 - \frac{\| \sum_t \mathbf{w}_{t,v} \|_2}{\sum_t \|\mathbf{w}_{t,v}\|_2 + \epsilon_{\mathbf{W}}} \right). \tag{21}$$

Let V_i be the set of sampled wall vertices. The target and predicted TAWSS fields are $\tau_i, \hat{\tau}_i$, and the corresponding OSI fields are $o_i, \hat{o}_i$. Their source-level errors are

$$E_i^{\text{TAWSS}} = \frac{\|\hat{\tau}_i - \tau_i\|_2}{\|\tau_i\|_2 + \epsilon_\tau}, \qquad E_i^{\text{OSI}} = |V_i|^{-1} \sum_{v \in V_i} |\hat{o}_i(v) - o_i(v)|. \tag{22}$$

If G_i and P_i are the equal-cardinality ground-truth and predicted top-10% TAWSS vertex sets, then hotspot overlap is $|G_i \cap P_i|/|G_i|$; hotspot error is TAWSS relative ℓ_2 error restricted to G_i. For peak timing and magnitude, use the spatial-mean magnitude curve $a_i(t) = |V_i|^{-1} \sum_v \|\mathbf{w}_{t,v}\|_2$ and define $t_i^* = \arg\max_t a_i(t)$ and $\hat{t}_i^* = \arg\max_t \hat{a}_i(t)$. Peak timing is the circular frame distance $\min(|\hat{t}_i^* - t_i^*|, N_t - |\hat{t}_i^* - t_i^*|)$ and peak-magnitude error is $|\hat{a}_i(\hat{t}_i^*) - a_i(t_i^*)|/(|a_i(t_i^*)| + \epsilon_a)$.

D.5 Source-level aggregation and uncertainty

Each reported metric z uses the nested reduction

$$\bar{z} = \frac{1}{N} \sum_{i=1}^{N} \frac{1}{M_i} \sum_{m=1}^{M_i} z_{im}, \qquad \mathcal{E}_{\mathrm{rel}} = \frac{1}{N} \sum_{i=1}^{N} \frac{1}{M_i} \sum_{m=1}^{M_i} e_{im}. \tag{23}$$

Here $M_i = 8$ for steady flow conditions and $M_i = 19$ for the stride-five $4 \to 4$ reset windows. Full-cycle metrics are computed once per source and averaged over the 79 sources. With this nested reduction, mean RMSE generally differs from the square root of mean MSE.

Core endpoint confidence intervals use 1,000 source-geometry cluster-bootstrap resamples and the 2.5th/97.5th percentiles; analyses with a different resampling count state it locally. Points, flow conditions, windows, and frames remain nested within their source geometries.

Training-seed summaries report sample SD across the runs identified in each table. Repeated adaptation from fixed initial weights describes adaptation-stage variability; it is reported separately from independent full-pipeline repeats.

E Extended Reference Results

The reference scores are reported in main-text Table 2; Appendix Table 16 gives parameter counts for both tasks. The following comparisons examine source-level differences and variability in source fine-tuning.

E.1 Paired-source comparisons

A lower source-mean error can combine improvements on some geometries with deteriorations on others. Figure 11 compares R1, R2, and R3 on the same sources and reports the fraction that improve. R1 and R2 are trained independently; R3 fine-tunes the R2 checkpoint on source fields.

Source fine-tuning lowers velocity error relative to R2 for every architecture and lowers reset-window WSS error for 8 of 9. Pressure changes are smaller and mixed. Most of the full R1-to-R3 difference is already present after descendant training.

E.2 Steady fine-tuning repeats

We measure source fine-tuning variability across random seeds while holding one descendant-pretrained checkpoint fixed for each architecture.

E.3 Steady source distributions and field examples

Figure 12 shows R3 error distributions across sources, with eight flow conditions averaged within each source.

F-FNO's R3 source-mean velocity RelL2 is 1.0005, close to the zero-velocity reference of one. GraphSAGE, Transolver, and voxel U-Net have lower medians, with substantial variation across sources. Pressure errors have longer right tails for nearly all architectures. Centered-pressure diagnostics in Appendix H separate spatial mismatch from the overall errors shown here.

Figure 13 shows where velocity and pressure predictions depart from the target fields. The source, camera, slice, and color scale are shared across models.

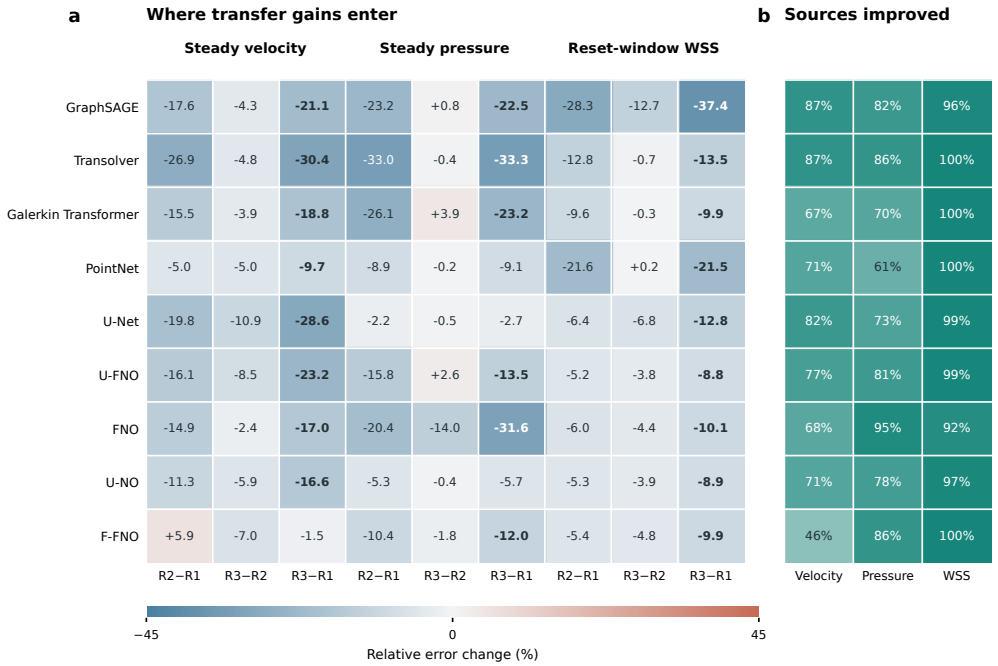


Figure 11: Paired comparisons of the three training settings across nine reference architectures. (a) Cells report relative error changes for R2 versus R1, R3 versus R2, and R3 versus R1; negative values denote lower error. Bold R3–R1 values have paired-source 95% bootstrap intervals excluding zero. The upper four rows are point/unstructured architectures and the lower five are voxel architectures. (b) Cells give the percentage of the same 79 source geometries improved by R3 relative to R1; darker fill denotes broader consistency. Figure 3 presents the GraphSAGE pool-size and allocation controls.

Table 19: Steady fine-tuning variability for three representative architectures. Each architecture uses one fixed seed-42 descendant-pretraining checkpoint and source fine-tuning seeds 42–44. Entries are held-out-source means ± sample SD across these seeds, conditional on the shared pretrained weights. RMSE is computed from decoded fields and reported in $\mathrm{m\,s^{-1}}$ for velocity and Pa for pressure. Lower is better.

Model	Representation	Field	RelL2	Physical-unit RMSE
PointNet	Point set	Velocity	0.891 ± 0.001	0.12606 ± 0.00009
		Pressure	0.773 ± 0.003	130.7 ± 0.2
GraphSAGE	16-NN graph	Velocity	0.654 ± 0.001	0.09486 ± 0.00001
		Pressure	0.560 ± 0.006	96.4 ± 0.3
U-Net	64^3 voxel	Velocity	0.704 ± 0.002	0.09795 ± 0.00010
		Pressure	0.795 ± 0.012	125.4 ± 0.2

F Descendant Pool Size and Allocation

The two aneurysm controls use GraphSAGE and the same source split. Pool-size runs change the available descendants while keeping sampling and update counts fixed. Allocation runs redistribute a fixed descendant count, then share a source fine-tuning stage. The airfoil study applies the allocation principle to a separate dataset and independently trained models.

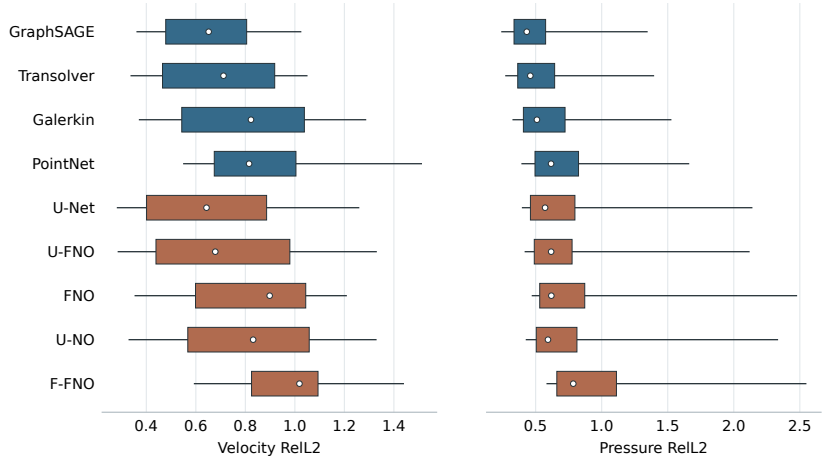


Figure 12: Source-level R3 steady relative-ℓ_2 distributions for the nine reference architectures. Blue denotes unstructured sampled-point architectures and orange voxel architectures. Each source contributes once after averaging its eight mass-flow conditions; boxes show quartiles and whiskers the 5th–95th percentiles.

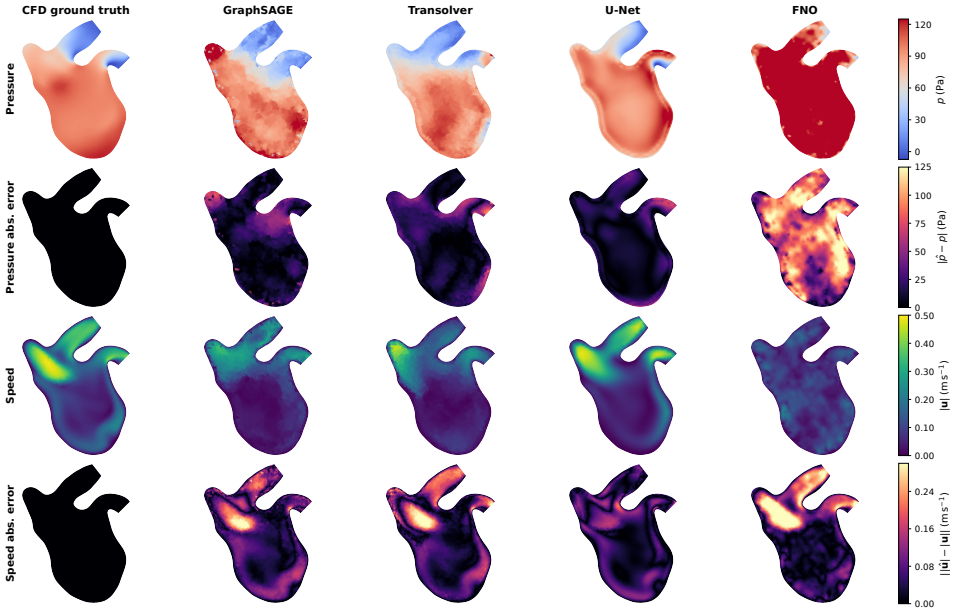


Figure 13: Steady-field comparison on a common plane through the 410,202-vertex, 137,745-cell internal VTU for held-out `real_0072` at $0.003\,\mathrm{kg\,s^{-1}}$. Rows show pressure in Pa, absolute pressure error, speed, and absolute speed error. The mostly-polyhedral mesh is tetrahedralized before slicing; all panels use the same plane triangulation and share a colorbar within each row. Point-model outputs are evaluated directly at 20,000 deterministic vertices and nearest-neighbor interpolated elsewhere for display. Voxel outputs are sampled trilinearly from the 64^3 grid. Cohort-level metrics appear in Tables 35 and 36.

F.1 Pool-size settings and results

The GraphSAGE pool-size control includes all 280 training sources and expands the accessible descendant pool from 280 to 560, 1,120, 2,238, 4,422, and 6,687 records. Each run draws 2,240

fields per epoch and performs 28,000 optimizer updates. Source-training normalization, validation selection, and deterministic test sampling are shared across the compared pools.

For each fixed pool, seeds 42–44 vary initialization and stochastic field sampling; sample SD summarizes the resulting training variability. Table 20 gives the pool means.

Table 20: GraphSAGE pool-size comparison on 79 held-out source geometries. All branches use 280 source lineages, 2,240 fields per epoch, 28,000 updates, and identical deterministic test samples. Values are source-level means ± training-seed SD across three seeds. Δ_{rel} is the paired relative change from source-only; "Wins" counts seeds improved on both fields. Pool membership is fixed across seeds at every size.

Training pool	Records	Velocity RelL2	Δ_{rel}	Pressure RelL2	Δ_{rel}	Wins
Source geometries	280	0.830 ± 0.005	–	0.731 ± 0.027	–	–
Descendant k=1	280	0.815 ± 0.002	-1.7%	0.706 ± 0.012	-3.3%	3/3
Descendant k=2	560	0.785 ± 0.002	-5.4%	0.680 ± 0.013	-6.8%	3/3
Descendant k=4	1,120	0.762 ± 0.003	-8.2%	0.663 ± 0.003	-9.2%	3/3
Descendant $k\leq$8	2,238	0.739 ± 0.002	-11.0%	$\mathbf{0.630 \pm 0.017}$	-13.8%	3/3
Descendant $k\leq$16	4,422	0.738 ± 0.006	-11.1%	0.635 ± 0.004	-13.0%	3/3
Descendant full pool	6,687	$\mathbf{0.734 \pm 0.008}$	-11.6%	0.633 ± 0.020	-13.2%	3/3

For GraphSAGE, most of the observed reduction occurs by approximately eight descendants per lineage, after which changes are small. All six tested descendant pools improve both endpoints in every paired seed. Each descendant is paired with a CFD field recomputed on its geometry, so the control evaluates the training value of these geometry–field pairs.

Table 21 lists the source-only and descendant results for each paired seed at $k = 4$. All three seeds use the same capped descendant membership.

Table 21: Seed-level GraphSAGE k=4 control on held-out source geometries. Both branches cover the same 280 source families and use equal numbers of sampled fields and updates, with the same normalization, validation, and deterministic test samples. The synthetic $k = 4$ membership is fixed across seeds. Metrics average eight flows per source; the final row reports mean (sample SD). Negative paired changes favor synthetic training.

Seed	Velocity RelL2			Pressure RelL2		
	Source only	Descendant k=4	Paired Δ_{rel}	Source only	Descendant k=4	Paired Δ_{rel}
42	0.8263	**0.7649**	**-7.4%**	0.7008	**0.6607**	**-5.7%**
43	0.8274	**0.7593**	**-8.2%**	0.7529	**0.6660**	**-11.6%**
44	0.8361	**0.7616**	**-8.9%**	0.7383	**0.6615**	**-10.4%**
Mean (SD)	0.830 (0.005)	**0.762 (0.003)**	**-8.2 (0.7)%**	0.731 (0.027)	**0.663 (0.003)**	**-9.2 (3.1)%**

F.2 Fixed-count allocation and common source fine-tuning

The fixed-budget lineage-allocation control instead holds the stage-1 pool at exactly 280 descendant records and compares 280×1, 140×2, 70×4, and 35×8 allocations, written as source lineages times descendants per lineage. Within each seed, the smaller lineage sets are nested inside the larger sets and use a shared within-lineage descendant ordering. Each branch trains on 2,240 descendant fields per epoch for 200 epochs (28,000 updates). All then fine-tune on the same 2,240 source fields per epoch for 100 epochs (14,000 updates). Normalization, validation, deterministic test sampling, and flow-condition sampling are fixed. GraphSAGE uses 4,096 points and is repeated with seeds 42–44.

GraphSAGE has its lowest mean velocity and stored-gauge pressure errors at the broadest of the four allocations. Table 23 separates stored-gauge pressure error from spatial pressure structure.

GraphSAGE's centered-pressure RelL2 exceeds one across these allocations, while its velocity predictions distinguish the allocations more clearly.

Table 22: GraphSAGE fixed-budget lineage breadth–depth allocation using 280 descendant records on the same 79 held-out source geometries. All branches use 2,240 stage-1 fields per epoch, 28,000 stage-1 updates, and the same 14,000-update source fine-tuning stage. Values are mean ± sample SD across seeds 42–44. Δ is the mean paired absolute change from 280×1; "wins" counts seeds with lower error than that reference. Lower is better.

	Velocity RelL2			Pressure RelL2		
Allocation	Mean ± SD	Δ	Wins	Mean ± SD	Δ	Wins
280×1	**0.799 ± 0.019**	–	–	**0.717 ± 0.032**	–	–
140×2	0.818 ± 0.012	+0.018	0/3	0.743 ± 0.027	+0.026	0/3
70×4	0.821 ± 0.014	+0.022	1/3	0.743 ± 0.029	+0.026	1/3
35×8	0.848 ± 0.022	+0.049	0/3	0.786 ± 0.040	+0.069	1/3

Table 23: GraphSAGE pressure-structure diagnostics for the fixed-280-descendant allocation control. Entries average source-balanced endpoints across seeds 42–44. Each checkpoint uses the same uniformly weighted fixed point samples as its primary allocation evaluation. Centered-pressure metrics subtract each field's spatial mean; a spatially constant pressure prediction has centered-pressure RelL2 approximately one. Lower is better.

Allocation	Stored-gauge RelL2	Centered-pressure RelL2	Centered-pressure RMSE (Pa)	Pressure-drop relative error
280×1	0.717	1.082	96.47	0.514
140×2	0.743	1.117	99.07	0.505
70×4	0.743	1.127	98.60	0.546
35×8	0.786	1.174	101.94	0.650

F.3 Airfoil construction, training, and allocation

The cross-domain study applies the lineage and exposure controls to airfoil geometries from AF-Bench (Liu et al., 2024). Its construction names link each class–shape transformation (CST) variant to a source airfoil, allowing descendants to inherit the source split directly. XFoil 6.97 computes the surface pressure coefficient at Reynolds number 10^6, Mach number 0.2, and 4° angle of attack. The result is represented on a canonical 256-point contour and evaluated by arc-length-weighted pressure-coefficient RelL2, averaged over source airfoils.

The split contains 280 training sources and 42 source-validation airfoils. Each descendant branch contains 280 fields allocated as 280×1, 140×2, 70×4, or 35×8. These four branches use 7,000 updates on the declared descendant allocation followed by 3,500 updates on the same 280 sources, with batch size 16 and source-only target normalization; the Source-only column is the separately trained reference recipe. Seeds 42–44 independently determine the nested lineage pool, data order, parameter initialization, and optimization. Evaluation uses all 47 unique solver-eligible sources remaining after cohort construction; none shares an exact geometry with the training or validation cohort.

GraphSAGE uses the airfoil implementation in `experiments/airfoil_protocol_transfer/train_airfoil.py`, with hidden width 128, depth parameter `n_layers=8`, and a symmetrized 16-nearest-neighbor graph on the contour coordinates. Both training stages use AdamW with weight decay 10^{-5} and a OneCycle schedule with peak learning rate 10^{-3} and warm-up fraction 0.3. Training minimizes arc-length-weighted MSE on normalized pressure coefficients.

A sweep on source-validation data selected a peak learning rate of 3×10^{-4} for Transolver. The 15 Transolver runs are evaluated on the 47 held-out airfoils. Figure 14 shows two comparisons, and Table 3 in the main text gives the full allocation sweep. Relative reductions are calculated from the unrounded means across seeds.

Among the four descendant allocations, GraphSAGE has its lowest mean at 280×1, whereas Transolver has its lowest at 35×8.

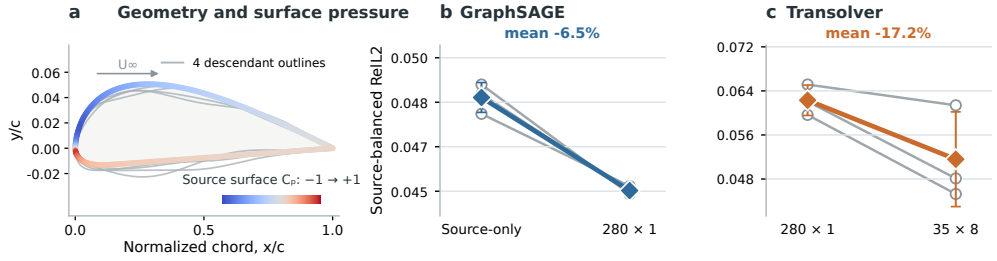


Figure 14: Cross-domain protocol transfer on source-edited airfoils. (a) The first training lineage in the frozen manifest: source airfoil `ag03` and its first four accepted CST descendants. The source surface is colored by its XFoil pressure coefficient at the declared flow condition; gray lines show descendant outlines. Separate x/c and y/c axis scales make the local edits visible. (b) GraphSAGE with broad descendant pretraining versus source-only training. (c) Transolver with the same 280-descendant budget allocated across 280 or 35 source lineages. Gray paths connect the same full-pipeline seed across conditions; colored diamonds and whiskers show mean $\pm$ training-seed SD for seeds 42–44. Both result panels use the same 47 held-out source airfoils; lower is better.

G WSS Forecasting and Temporal Diagnostics

The WSS analyses compare local-history predictors with spatial models, then examine how training feedback and forecast length affect rollout. All use the same held-out source geometries. Cycle metrics and input interventions assess what the resulting forecasts preserve and which observations they use.

G.1 Temporal reference baselines

Copy-last persistence repeats the final observed WSS frame. Linear extrapolation fits a line through the current four-frame history independently at each point and component, without fitting parameters across training cases.

History+phase ridge regression instead fits shared coefficients in closed form on deterministic subsets of the source-training cohort. Its 16 features comprise 12 normalized WSS history components, phase, sine and cosine of phase, and an intercept. The normal-equation penalty is $10^{-6}N_{\text{fit}}$, where $N_{\text{fit}} = 13{,}615{,}104$ is the number of fitting rows; the intercept is unpenalized. These coefficients remain fixed during evaluation.

All three baselines use each wall point's own history throughout the sequence, without explicit coordinates or interactions between points.

PointwiseMLP. PointwiseMLP provides a nonlinear residual counterpart to the ridge baseline. It shares weights across points, while each output depends only on that point's registered history and phase. It maps the 13 history-and-phase inputs to width 128, applies four pre-normalized residual multilayer perceptron (MLP) blocks with expansion two and Gaussian error linear unit (GELU) activation, and decodes one WSS vector per point (267,139 trainable parameters).

R1 uses AdamW, weight decay 10^{-5}, a 200-epoch OneCycle schedule with peak learning rate 10^{-3}, batch size 32, and independent seeds 42, 43, and 44. The checkpoint with the lowest four-step autoregressive RelL2 on validation sources is selected. Rollout predicts one frame at a time for 96 steps.

PointwiseMLP seed 42 improves rollout error over persistence on 72/79 sources. Top-10% overlap decreases on every source. The paired records are in `data/validation/pointwise_persistence_paired.json`. All three PointwiseMLP seeds have lower mean rollout error than persistence, although the metric values vary across seeds.

Table 24: Temporal reference baselines and an exploratory PointwiseMLP diagnostic. Persistence and linear extrapolation require no training-data fit; history+phase ridge regression is fit in closed form on source-training data. Bracketed entries give source means and 95% source-bootstrap CIs over the 79-source test set. The final row reports mean ± training-seed SD over three independently trained and validation-selected PointwiseMLP pipelines.

Method	Window RelL2	Rollout RelL2	Mean cumulative RelL2
Copy-last persistence	0.2580 [0.2482, 0.2679]	0.8806 [0.8785, 0.8828]	0.7389 [0.7370, 0.7407]
Linear extrapolation	0.3426 [0.3229, 0.3618]	0.9929 [0.9802, 1.0135]	0.8040 [0.7962, 0.8152]
History+phase ridge, no coordinates	0.2706 [0.2613, 0.2810]	0.9911 [0.9888, 0.9937]	0.8624 [0.8582, 0.8668]
PointwiseMLP R1, seed 42	0.1463 [0.1341, 0.1596]	0.7797 [0.7614, 0.7986]	0.6446 [0.6282, 0.6612]
PointwiseMLP R1, 3-seed mean ± SD	0.1459 ± 0.0022	0.7346 ± 0.1047	0.6013 ± 0.0869

G.2 Standard reset-window and rollout results

Under reset-window evaluation, Transolver and Galerkin Transformer are nearly tied within the unstructured track under both RelL2 and decoded RMSE (Table 37). U-Net has the lowest error among the voxel models.

We evaluate the standard R1, R2, and R3 checkpoints over the 96-step rollout. Their largest error increase occurs near the rapid transition at predicted step 19.

Table 25 reports seed-42 R1–R3 rollouts for Transolver and voxel U-Net, the two models with rollout results for all three settings. R2 predictions are decoded with descendant-training normalization; R1 and R3 use source-training statistics.

Panel (b) reports paired rollout differences, intervals, relative changes, and source improvement fractions. The intervals describe variation among test sources for these fixed checkpoints. Statistics for all metrics are retained in `data/validation/transient_transfer_rollout.json`. R2 rollout is available only for seed 42; independent R1/R3 training repeats follow below.

For Transolver seed 42, R3 lowers the mean rollout error, although only 34.2% of sources improve. Each of the three independent R3 runs also has lower source-mean error than its paired R1 run (Table 26).

G.3 Independent R1/R3 training repeats

To measure training variability, we independently train R1 and the complete descendant-to-source pipeline with seeds 42–44 (Table 26). Each R3 run starts from its own R2 checkpoint, and sample SD summarizes variability across the resulting pipelines.

G.4 Feedback training and forecast horizon

Training feedback determines which frames enter the history. The forecast horizon determines how many future frames contribute to each update. We compare both choices before evaluating fixed R1 and R3 initializations under the same long-window adaptation (Section G.5).

Scheduled sampling starts from the same architecture-specific R2 checkpoint as core R3 fine-tuning and retains its 100-epoch source-geometry schedule, $H = F = 4$, and default seed 42. At epoch e, the feedback probability is

$$\pi_e = 0.5\, e/100, \qquad e = 1, \ldots, 100. \tag{24}$$

At each autoregressive target step in a minibatch, one Bernoulli draw is shared by the batch; success appends the detached prediction and failure appends the ground-truth frame. Each reported SS

Table 25: R1–R3 checkpoints under reset-window and 96-step WSS evaluation on the same 79 held-out sources, using seed 42. Lower is better except top-10% overlap. Panel (b) reports paired-source rollout changes; negative values favor the later regime. Table 26 reports independent pipeline repeats across training seeds.

(a) Endpoint estimates

Model	Regime	Reset RelL2	Rollout RelL2	TAWSS rel.	OSI abs.	Top-10% overlap
Transolver	R1	0.1253	1.5907	1.2793	0.0383	0.7898
	R2	0.1092	0.9810	0.8873	0.0602	0.8211
	R3	0.1084	0.9836	0.8785	0.0569	0.8240
Voxel U-Net	R1	0.2369	0.9118	0.7673	0.0461	0.6128
	R2	0.2216	0.9450	0.8296	0.0380	0.4118
	R3	0.2064	0.9824	0.8740	0.0381	0.6117

(b) Paired rollout changes

Model	Comparison	Rollout difference	Relative change	95% paired-source CI	Sources improved
Transolver	R2–R1	-0.6097	-38.3%	[-1.2064, -0.1579]	31.6%
	R3–R1	-0.6071	**-38.2%**	[-1.1686, -0.1435]	34.2%
	R3–R2	+0.0026	+0.3%	[-0.0284, +0.0329]	50.6%
Voxel U-Net	R2–R1	+0.0333	+3.6%	[+0.0159, +0.0506]	27.8%
	R3–R1	+0.0707	**+7.8%**	[+0.0404, +0.1071]	21.5%
	R3–R2	+0.0374	+4.0%	[+0.0132, +0.0636]	32.9%

Table 26: Independent full-pipeline replications for transient transfer. Each seed trains R1 from random initialization, trains its own R2 checkpoint, and initializes R3 from that checkpoint. Panel (a) reports vertex-sampled RelL2; Δ is paired within seed. The final rows give mean $\pm$ sample SD across three training seeds. Panel (b) reports cycle endpoints as mean $\pm$ sample SD. All evaluations use the same 79 sources. R2 rollout was not repeated and remains in Table 25 as a seed-42 diagnostic.

(a) Reset-window and 96-step rollout RelL2

Model	Seed	R1 reset	R3 reset	Δ	R1 rollout	R3 rollout	Δ
Transolver	42	0.1253	0.1084	-0.0169	1.5907	0.9836	-0.6071
	43	0.1272	0.1091	-0.0181	1.1231	0.9467	-0.1764
	44	0.1305	0.1083	-0.0222	1.1219	0.9673	-0.1546
	Mean	0.1276	0.1086	-0.0190	1.2786	0.9659	-0.3127
	$\pm$ SD	$\pm$0.0026	$\pm$0.0004	$\pm$0.0028	$\pm$0.2703	$\pm$0.0185	$\pm$0.2552
Voxel U-Net	42	0.2369	0.2064	-0.0304	0.9118	0.9824	+0.0707
	43	0.2469	0.2098	-0.0371	0.9835	0.9509	-0.0326
	44	0.2565	0.2085	-0.0480	0.9676	0.9348	-0.0328
	Mean	0.2468	0.2083	-0.0385	0.9543	0.9560	$+0.0018$
	$\pm$ SD	$\pm$0.0098	$\pm$0.0017	$\pm$0.0089	$\pm$0.0377	$\pm$0.0242	$\pm$0.0597

(b) Cycle endpoints across training seeds

		TAWSS rel.		OSI abs.		Top-10% overlap	
Model	Seeds	R1	R3	R1	R3	R1	R3
Transolver	42–44	1.0263 $\pm$0.2354	0.7900 $\pm$0.0893	0.0446 $\pm$0.0055	0.0393 $\pm$0.0154	0.7923 $\pm$0.0087	0.7875 $\pm$0.0335
Voxel U-Net	42–44	0.7756 $\pm$0.0330	0.8474 $\pm$0.0264	0.0482 $\pm$0.0029	0.0384 $\pm$0.0064	0.5198 $\pm$0.0853	0.5739 $\pm$0.0331

row is one validation-selected checkpoint; its rollout endpoints are reported with the other temporal interventions in Table 29.

The long-window variants retain four history frames, predict $F = 16$ targets, and reuse detached predictions as full feedback. The Transolver variant is the $F = 16$ full-feedback cell of the factorial below. The U-Net replication starts from its corresponding fixed R3 checkpoint and uses the same batch size eight, learning rate 10^{-4}, and validation selection with a 20-epoch schedule. For each model, the reported mean and sample SD summarize three adaptation seeds from one fixed R3 initialization.

G.4.1 Horizon–feedback factorial

Every run in the horizon–feedback factorial starts from the same Transolver R3 checkpoint. The factorial crosses training horizon $F \in \{4, 8, 16\}$ with teacher forcing or full stop-gradient feedback. All 18 runs use four history frames, batch size eight, AdamW with maximum learning rate 10^{-4}, and a complete 30-epoch OneCycle schedule; the three repeats vary only the adaptation seed.

Longer horizons predict more training frames within the common 30-epoch schedule. Figure 15 compares rollout errors, and Table 27 gives the reset and cycle-level endpoints.

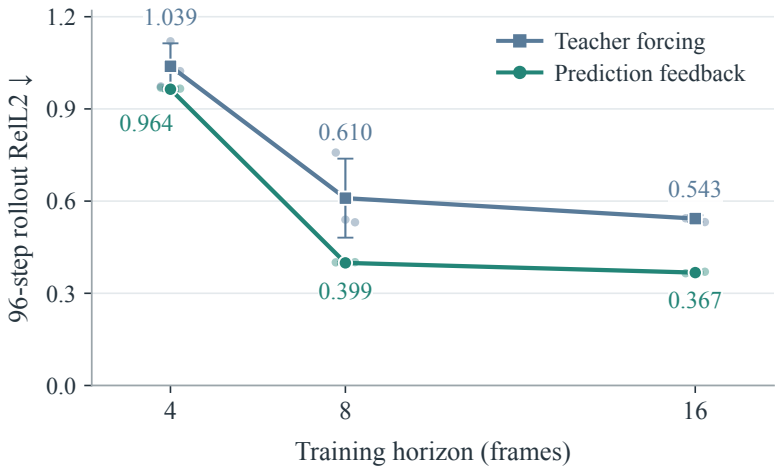


Figure 15: Transolver rollout accuracy after 30 epochs of adaptation from one shared R3 checkpoint. Each training window predicts F frames, with either observed or predicted frames appended to the history. Small dots are individual adaptation seeds; markers show means with sample SD. Table 27 gives the complete metrics.

At the common 30-epoch budget, increasing F lowers rollout error under both teacher forcing and full feedback, and full feedback is lower at every tested horizon. Reset-window RelL2 remains between 0.1073 and 0.1090, so the separation appears primarily in uninterrupted rollout.

G.5 Initialization under matched long-window adaptation

The initialization comparison gives fixed seed-42 Transolver R1 and R3 checkpoints identical $F = 16$ feedback training. The six runs use paired adaptation seeds 42–44, eight epochs, batch size eight, and a complete OneCycle schedule with peak learning rate 10^{-4}. Each run predicts 602,752 training frames. Checkpoints are selected by source-validation error at epochs five and eight; test evaluation is omitted during training. Table 28 reports results on the same 79 sources.

R3 initialization lowers rollout error in every paired seed, with improvements on 72, 74, and 72 of the 79 sources. Its mean reduction is 20.8%; a source-bootstrap interval for the seed-averaged R3–R1 difference is $[-0.1250, -0.0735]$. TAWSS error also decreases, while OSI error rises slightly. The complete protocol and per-source results are recorded under `experiments/transient_r1_r3_f16_20260907/`.

Table 27: Three-seed Transolver horizon–feedback factorial from one shared R3 initialization. All settings use 30 epochs. Entries are mean ± adaptation-seed sample SD. Lower is better except top-10% overlap.

F Feedback	Reset $4\to4$	96-step rollout	TAWSS rel.	OSI abs.	Top-10% overlap
4 Teacher forcing	0.1087 ±0.0001	1.0387 ±0.0747	0.9245 ±0.0693	0.0561 ±0.0002	0.816 ±0.003
4 Full feedback	**0.1073 ±0.0001**	0.9640 ±0.0064	0.8809 ±0.0126	0.0422 ±0.0005	**0.830 ±0.003**
8 Teacher forcing	0.1088 ±0.0001	0.6096 ±0.1286	0.4263 ±0.1264	**0.0273 ±0.0003**	0.794 ±0.007
8 Full feedback	0.1078 ±0.0003	0.3990 ±0.0035	0.2416 ±0.0093	0.0282 ±0.0000	0.827 ±0.001
16 Teacher forcing	0.1090 ±0.0001	0.5431 ±0.0109	0.3573 ±0.0148	0.0281 ±0.0003	0.802 ±0.004
16 Full feedback	0.1084 ±0.0001	**0.3673 ±0.0025**	**0.2088 ±0.0017**	0.0283 ±0.0001	0.830 ±0.001

Table 28: Transolver initialization comparison after identical eight-epoch $F = 16$ full-feedback adaptation. Entries are source-level means ± sample SD over three adaptation seeds, conditional on one fixed upstream checkpoint per initialization. The final column is R3 minus R1. Lower is better except hotspot overlap.

Endpoint	R1 initialization	R3 initialization	Difference
Reset RelL2	0.12811 ± 0.00060	0.10826 ± 0.00004	-0.01986
96-step rollout RelL2	0.46840 ± 0.01369	0.37076 ± 0.00390	-0.09764
Mean cumulative RelL2	0.38256 ± 0.00826	0.30933 ± 0.00297	-0.07323
TAWSS relative error	0.32239 ± 0.02310	0.21591 ± 0.00458	-0.10649
OSI absolute error	0.02747 ± 0.00025	0.02836 ± 0.00013	$+0.00089$
Top-10% overlap	0.83226 ± 0.00015	0.83737 ± 0.00027	$+0.00512$

G.6 Cycle metrics, source distributions, and field examples

For uninterrupted forecasts, Table 29 compares cycle and spatial endpoints for the temporal references and feedback variants.

U-Net has low adaptation-seed variability but still has large errors through the cardiac transition, with a cumulative-error rise at the same phase as the short-horizon checkpoint.

Most sources have high rollout errors and low predicted amplitudes under standard R3 or scheduled sampling. Galerkin's pronounced right tail raises its mean above its median. Transolver F=16 lowers rollout, TAWSS, and peak-magnitude errors. Persistence has the highest median top-10% overlap, despite a larger mean trajectory error than Transolver F=16.

These distributions complement the mean trajectories in Figure 16b. Most standard neural models show an abrupt error increase near the rapid transition; Transolver F=16 accumulates error more gradually.

G.7 Coordinate and history interventions

The intervention study evaluates fixed reset windows after perturbing coordinates, histories, or both at inference. Coordinate permutation reassigns xyz across wall points while leaving each WSS history and target paired. Coordinate zeroing sets the explicit position inputs to zero. History permutation instead breaks the correspondence between each wall point and its local WSS trace. A joint coordinate–history permutation, undone before scoring, checks permutation equivariance. These interventions evaluate the trained Transolver and Galerkin Transformer checkpoints.

Table 29: Exploratory full-cycle transient diagnostics. Lower is better except top-10% overlap; peak timing uses circular frame distance. PointwiseMLP entries average three independently trained R1 pipelines. F=16 entries average three adaptation seeds from one fixed R3 initialization: 30 epochs for Transolver and 20 for U-Net. The eight-epoch initialization comparison is in Table 28. The remaining neural-model rows use single validation-selected checkpoints.

(a) Trajectory and cycle errors

Method	Rollout RelL2	Mean cumulative RelL2	TAWSS rel.	OSI abs.
Persistence	0.8806	0.7389	0.7254	0.0298
Linear extrapolation	0.9929	0.8040	0.8349	0.1482
History+phase ridge	0.9911	0.8624	0.9045	0.0696
PointwiseMLP R1	0.7346	0.6013	0.5694	0.0287
U-Net R3	0.9824	0.8171	0.8740	0.0381
U-Net SS(0.5)	0.9711	0.8084	0.8670	0.0364
U-Net F=16	0.9326	0.7809	0.8486	0.0395
Transolver R3	0.9836	0.8017	0.8785	0.0569
Transolver SS(0.5)	0.9475	0.7771	0.8836	0.0550
Transolver F=16	0.3673	0.3073	0.2088	0.0283
Galerkin R3	1.1258	0.8519	0.9340	0.0371
Galerkin SS(0.5)	1.0729	0.8155	0.8242	0.0356

(b) Hotspot and peak errors

Method	Top-10% rel.	Top-10% overlap	Peak time (frames)	Peak mag. rel.
Persistence	0.7158	0.8466	26.97	0.9415
Linear extrapolation	0.8421	0.6388	27.62	0.9117
History+phase ridge	0.9278	0.7562	21.57	0.9213
PointwiseMLP R1	0.5640	0.5194	0.89	0.3558
U-Net R3	0.8541	0.6117	17.82	0.9236
U-Net SS(0.5)	0.8504	0.6294	17.96	0.9275
U-Net F=16	0.8476	0.7371	26.25	0.9410
Transolver R3	0.8749	0.8240	24.58	0.9222
Transolver SS(0.5)	0.8814	0.8297	25.92	0.9242
Transolver F=16	0.1769	0.8299	0.20	0.1256
Galerkin R3	0.8276	0.7155	18.00	0.8933
Galerkin SS(0.5)	0.7147	0.7519	18.00	0.7372

For the raw-coordinate Transolver checkpoint, coordinate permutation changes source-mean error by -2.2×10^{-6} and zeroing by -1.4×10^{-5}; both paired intervals cross zero. Galerkin Transformer changes by $+2.7\times10^{-6}$ and -3.4×10^{-7}. History permutation raises the two errors by 1.2552 and 1.2540, and every source degrades. Under the reset protocol, these checkpoints draw most of their predictive signal from the registered WSS histories, with little incremental use of explicit xyz.

H Representation and Physical-Field Diagnostics

This section reports how weighting, pressure definitions, input coordinates, and point sampling affect the reference results. Definitions are in Section D; the original sampling and input conventions are in Section C.

H.1 Native-volume and wall-area weighting

The sensitivity analysis reevaluates representative R1/R3 checkpoints with native-mesh weights and pressure diagnostics (Table 30). Sampling domains and source-level reduction follow Appendices C

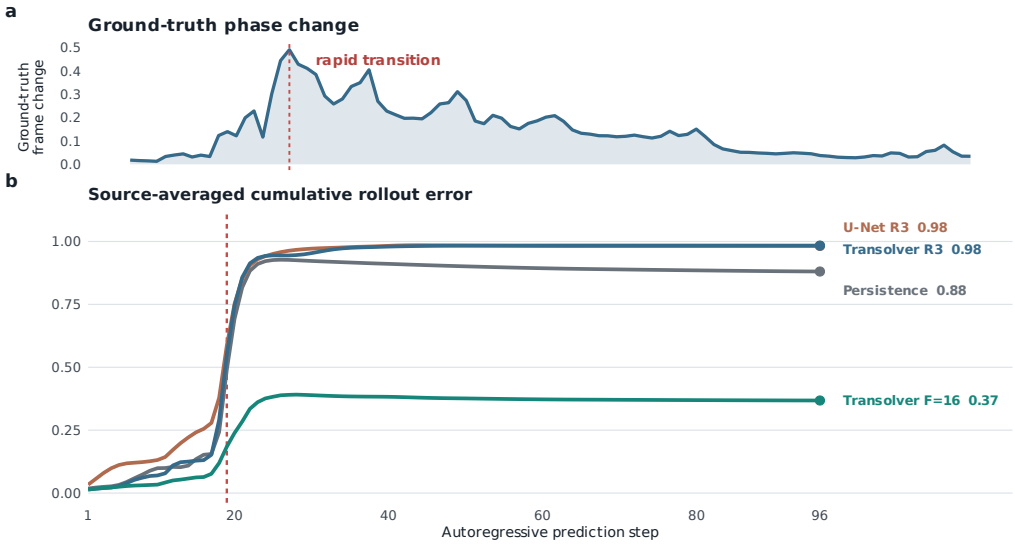


Figure 16: Exploratory 96-step rollout diagnostics aligned with the cardiac phase. (a) Mean ground-truth frame change peaks near predicted step 19. (b) Source-mean cumulative error for four reference methods over the same rollout, with step-96 values labeled directly. The standard neural pipelines separate from 16-step full-feedback Transolver near the rapid transition. Additional exploratory methods are reported in Table 29.

and D; intervals resample the 79 test sources. The comparison measures sensitivity to uniform weighting of stored or sampled vertices.

Table 30: Representative quadrature and pressure-gauge sensitivity on the 79 held-out sources. Panel (a) compares the primary, uniformly weighted vertex/mask evaluation with native-VTU lumped cell-volume weighting; uniform voxel volumes cancel exactly. Centered-pressure RelL2 ($\mathcal{E}_p^{\mathrm{center}}$) subtracts each field's weighted spatial mean. The final two columns are sampled inlet–outlet pressure-drop absolute error in Pa and relative error; both are unavailable for the voxel representation. Panel (b) uses native wall-polygon area weights. Negative change favors R3.

(a) Steady velocity and pressure

Model	Track	Regime	$\mathcal{E}_u$	$\mathcal{E}_u^{(V)}$	$\mathcal{E}_p$	$\mathcal{E}_p^{(V)}$	$\mathcal{E}_p^{\mathrm{center}}$	Drop abs. (Pa)	Drop rel.
GraphSAGE	Points	R1	0.8269	0.8011	0.7131	0.6769	1.1994	186.6	0.5317
GraphSAGE	Points	R3	0.6521	0.6395	0.5525	0.5287	0.9211	137.7	0.4176
Transolver	Points	R1	1.0031	1.0009	0.8672	0.8021	1.0228	401.6	0.9962
Transolver	Points	R3	0.6979	0.6714	0.5783	0.5062	0.8614	124.5	0.3864
U-Net	Voxel	R1	0.9867	0.9867	0.8147	0.8147	1.0174	–	–
U-Net	Voxel	R3	0.7050	0.7050	0.7930	0.7930	1.1333	–	–
FNO	Voxel	R1	1.0099	1.0099	1.3334	1.3334	1.2366	–	–
FNO	Voxel	R3	0.8387	0.8387	0.9126	0.9126	1.1802	–	–

(b) Reset-window WSS

Model	Track	R1 vertex	R1 area	R3 vertex	R3 area	Area-weighted R3–R1
Transolver	Points	0.1253	0.1303	0.1084	0.1136	-12.9%
Galerkin Transformer	Points	0.1210	0.1251	0.1090	0.1139	-9.0%
U-Net	Voxel	0.2369	0.2404	0.2064	0.2102	-12.6%
FNO	Voxel	0.2387	0.2412	0.2145	0.2186	-9.4%

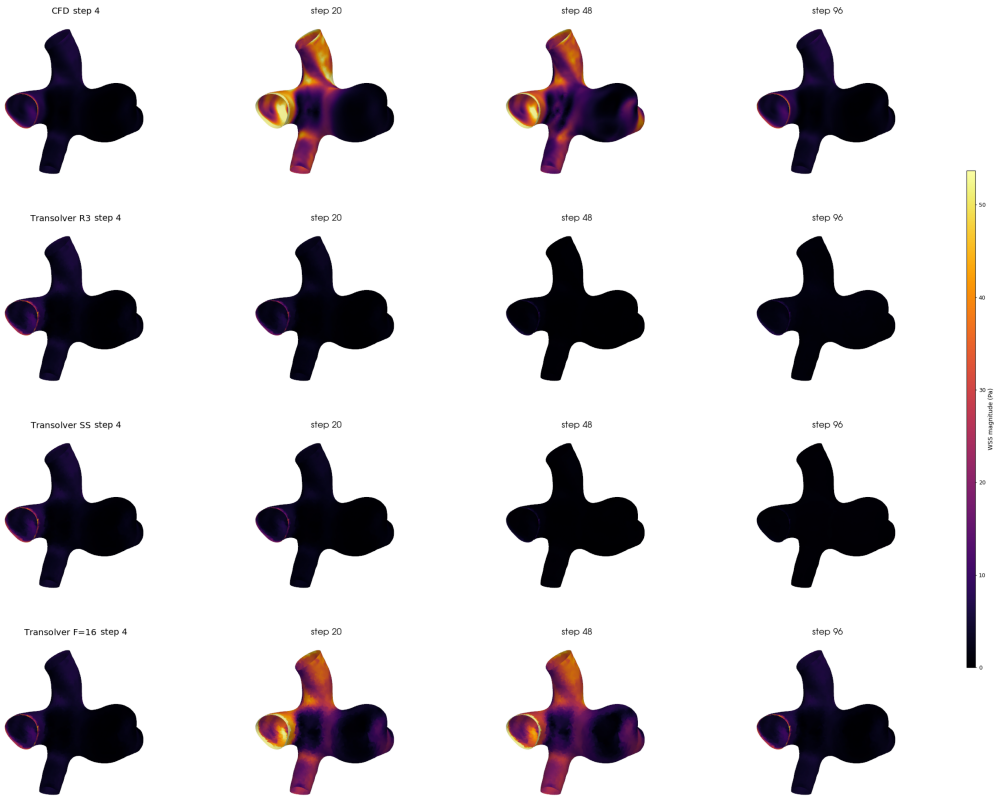


Figure 17: WSS evolution for an illustrative held-out case at rollout steps 4, 20, 48, and 96. Rows compare CFD, standard Transolver R3, scheduled sampling, and $F = 16$ full-feedback adaptation. All panels use a shared scale derived from ground truth. Values at evaluation vertices are shown directly; values elsewhere are nearest-neighbor interpolated for display. Table 29 reports cohort-level trajectory and hemodynamic metrics.

With volume weighting, R3 has lower velocity and stored-gauge pressure error for all four representative steady models. Wall-area weighting gives lower R3 WSS error for all four transient models.

H.2 Pressure structure and pressure-drop results

Centered-pressure RelL2 varies across models: GraphSAGE and Transolver improve, FNO has a lower unit-box R3 point estimate, and voxel U-Net does not improve. The FNO rerun with centered physical coordinates has a paired interval spanning zero. Both unstructured models also have lower pressure-drop error under R3.

The models with the lowest pressure RelL2 have negative mean per-case R^2. RelL2 normalizes error by the target-field norm, RMSE retains physical units, and R^2 uses centered target energy (Section D). For an individual case, negative R^2 means that residual energy exceeds the squared error of predicting its target mean. Centered-pressure error and sampled-edge gradients assess errors in spatial variation; the common-plane comparison shows where predictions depart from the target fields.

H.3 Voxel coordinate-scale sensitivity

The unit-box voxel reference omits the stored bounding-box scale. The physical-coordinate sensitivity reruns the complete steady R1/R2/R3 pipelines for U-Net and FNO with centered physical coordinates, retaining the original occupancy, grid resolution, exported point domain, splits, nor-

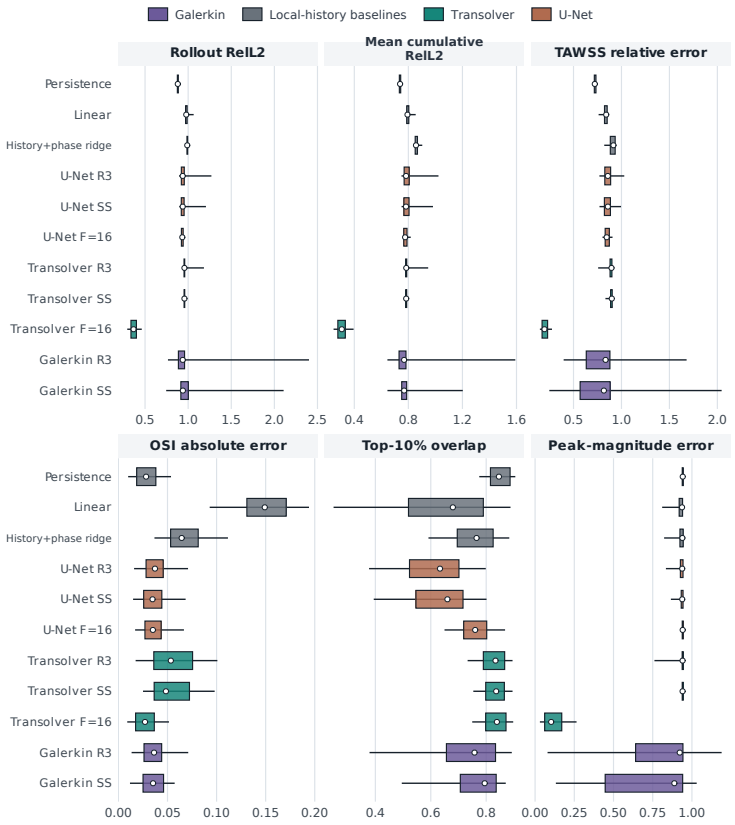


Figure 18: Exploratory source-level 96-step rollout distributions for temporal reference baselines and the R3, scheduled-sampling, and F=16 interventions. Each panel uses the metric's natural scale; "Trajectory AUC" denotes mean cumulative RelL2. Boxes show quartiles and whiskers the 5th–95th percentiles. Top-10% overlap is higher-is-better; all other panels are errors.

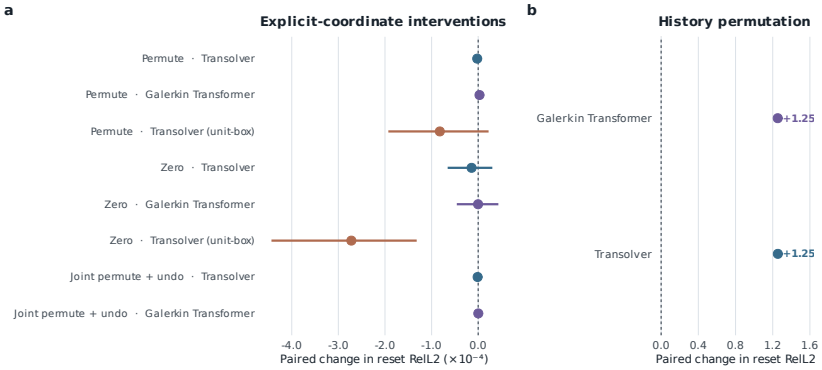


Figure 19: Explicit-coordinate and registered-history interventions on point-attention reset checkpoints. (a) Changes from coordinate permutation, coordinate zeroing, and the joint permutation–undo check for the two raw-coordinate checkpoints, shown in units of 10^{-4}. The panel also includes a unit-box Transolver sensitivity. (b) History-only permutation on the natural RelL2 scale. Breaking the WSS-history correspondence raises error by about 1.255, whereas explicit-coordinate and joint-equivariance changes remain near zero. Points are mean source-paired changes and bars are 95% source-bootstrap intervals over the same 79 held-out sources.

malization protocol, optimizer schedules, and test sources. Checkpoint selection uses the source-validation cohort. These runs change coordinate scale; the cell-connected point-domain evaluation follows in Section H.4.

Table 31: Sensitivity to centered physical coordinates on 79 held-out sources. Panel (a) reports source-averaged point estimates. Panel (b) gives paired R3–R1 changes with 10,000 source-bootstrap resamples; negative values favor R3. These reruns restore the stored longest-side physical scale. The main voxel table reports the original unit-box checkpoints.

(a) R1/R2/R3 endpoints

Model	Regime	Velocity RelL2	Stored-gauge pressure RelL2	Centered-pressure RelL2
U-Net	R1	0.9803	1.5510	1.3582
	R2	0.8209	0.7442	1.0601
	R3	0.7264	0.6702	0.9786
FNO	R1	1.0093	1.3407	1.2235
	R2	0.8585	1.0012	1.2836
	R3	0.8403	0.9276	1.2037

(b) Paired R3–R1 effects

Model	Endpoint	R3–R1 difference	Relative change	95% paired-source CI	Sources improved
U-Net	Velocity	-0.2539	-25.9%	$[-0.3118, -0.1950]$	82.3%
	Stored-gauge pressure	-0.8809	-56.8%	$[-1.0439, -0.7367]$	98.7%
	Centered-pressure RelL2	-0.3796	-28.0%	$[-0.4967, -0.2793]$	89.9%
FNO	Velocity	-0.1690	-16.7%	$[-0.2303, -0.1077]$	68.4%
	Stored-gauge pressure	-0.4131	-30.8%	$[-0.5924, -0.2803]$	94.9%
	Centered-pressure RelL2	-0.0198	-1.6%	$[-0.0835, +0.0438]$	60.8%

With centered physical coordinates, U-Net's R3 endpoint is lower than R1 for velocity, stored-gauge pressure, and centered-pressure RelL2, with paired intervals excluding zero; its unit-box centered-pressure RelL2 instead rises. FNO retains velocity and stored-gauge pressure reductions, but its centered-pressure RelL2 change is inconclusive. Coordinate scale changes the direction of U-Net's centered-pressure comparison in this steady task. Centered physical coordinates in metres are recommended for new experiments.

H.4 Cell-connected point-domain evaluation

Some exported volume points are not referenced by any CFD cell and store zero velocity and pressure. Across all 280 training and 42 validation sources at $0.002\,\mathrm{kg\,s^{-1}}$, their median shares are 6.28% and 6.26%. Native-cell probes on four sources locate more than 99% of these coordinates inside active cells, with median interpolated speeds of 0.0377–$0.1164\,\mathrm{m\,s^{-1}}$.

We define valid supervised points as the unique vertices referenced by mesh cells, preserving connected wall vertices and their physical zero velocities. Selection depends on mesh connectivity, not on field values. Cell-connected preprocessing applies this domain before point sampling, estimation of training normalization statistics, and voxel interpolation.

For new steady point-model training, `scripts/train_steady_physical.py` selects the `cell_connected` domain. Voxel construction through `data/build_voxel.py` uses the same default. The workflow in `docs/STEADY_POINT_DOMAIN.md` specifies normalization and the matching training and evaluation commands; voxel training additionally selects `physical_centered` coordinates. The archived reproduction commands use `all`, matching the original arrays used to train the reported steady reference and allocation checkpoints. The physical-coordinate reruns above also use this original point domain.

To separate scoring effects from changes in model inputs, we hold the six GraphSAGE allocation checkpoints and their normalization fixed and evaluate all 79 sources at eight flow conditions.

From each original deterministic 4,096-point sample, we first restrict scoring to cell-connected entries while retaining all inputs. We then remove orphan inputs and rebuild the graph, evaluating at the same active query IDs and targets. The second comparison changes graph neighborhoods and GraphSAGE batch statistics as well as input membership.

Table 32: Effects of scoring and input point domains on the two GraphSAGE allocations. Values are source-mean RelL2 $\pm$ sample SD across three training seeds. Model weights are fixed during evaluation. The two cell-connected evaluations use the same subset of the original query points.

	Velocity		Stored-gauge pressure	
Evaluation	280×1	35×8	280×1	35×8
Original inputs and scoring	0.7993 ± 0.0186	0.8480 ± 0.0218	0.7167 ± 0.0324	0.7856 ± 0.0397
Active scoring, original inputs	0.7766 ± 0.0178	0.8265 ± 0.0205	0.6620 ± 0.0291	0.7327 ± 0.0431
Active inputs and scoring	0.7788 ± 0.0186	0.8274 ± 0.0216	0.6705 ± 0.0334	0.7363 ± 0.0443

The point domain changes the absolute errors, while both mean endpoints remain lower for 280×1 in all three evaluations. Velocity is lower in all three paired seeds and pressure in two, matching their original directions. These comparisons establish the ordering for the six fixed checkpoints on valid queries. Training on the cell-connected domain remains to be evaluated under the same allocation budgets.

H.5 Wall-point sampling sensitivity

The main transient protocol evaluates 4,096 deterministic wall vertices per source. Table 33 repeats the reset-window evaluation with 8,192 vertices and with every available wall vertex. The two attention models change by at most 2.4×10^{-4} RelL2, while full-surface evaluation spans 5,437–29,686 vertices per source. The reset-window ranking is unchanged across these evaluation point budgets.

Table 33: Transient reset-window sensitivity to wall-point evaluation density. All columns evaluate the same R3 checkpoint on the same 79 held-out sources; lower RelL2 is better.

Model	Fixed 4,096	Fixed 8,192	Full surface
Transolver	0.108406	0.108419	0.108648
Galerkin Transformer	0.109043	0.108883	0.108975

H.6 Steady fine-tuning recipe sensitivity

The steady R3 comparisons vary the fine-tuning learning rate or target normalization one at a time (Table 34). Across the seven models, each alternative changes velocity RelL2 by at most 0.0158 and pressure RelL2 by at most 0.0354. The direction depends on the model and endpoint: a setting that lowers pressure error can raise velocity error.

H.7 Auxiliary metrics

The following tables report amplitude errors, directional errors, and pressure R^2 using the definitions in Appendix D. Metrics are computed from decoded fields: pressure RMSE is in Pa and velocity RMSE in $\mathrm{m\,s^{-1}}$. Each model is evaluated on its specified domain before any interpolation for visualization.

Table 34: Targeted steady R3 sensitivity runs. Cells are velocity / pressure RelL2. The base setting uses learning rate 10^{-4} and source-training normalization; the other columns change one choice at a time.

Track	Model	Base R3	Learning rate 5×10^{-4}	Synthetic normalization
Unstructured	Galerkin Transformer	0.8150 / 0.6667	0.8227 / 0.6880	0.8143 / 0.6548
Unstructured	GraphSAGE	0.6521 / 0.5525	0.6550 / 0.5465	0.6542 / 0.5421
Unstructured	PointNet	0.8899 / 0.7718	0.8945 / 0.7598	0.9021 / 0.7687
Unstructured	Transolver	0.6979 / 0.5783	0.6997 / 0.5875	0.6997 / 0.5920
Voxel	FNO	0.8387 / 0.9126	0.8405 / 0.9278	0.8414 / 0.9106
Voxel	U-FNO	0.7568 / 0.7925	0.7603 / 0.8168	0.7622 / 0.8279
Voxel	U-Net	0.7050 / 0.7930	0.7208 / 0.8013	0.7086 / 0.7874

Table 35: R3 steady velocity diagnostics on 79 held-out source geometries. Metrics are computed from decoded fields, averaged over eight flow conditions within each source, and then averaged across sources. RelL2 brackets are 95% source-bootstrap CIs. MSE has units $\mathrm{m}^2\,\mathrm{s}^{-2}$; RMSE, MAE, and magnitude MAE have units $\mathrm{m}\,\mathrm{s}^{-1}$.

(a) Field errors

Model	RelL2 95% CI	Mean MSE	Mean RMSE	Mean MAE
Unstructured				
GraphSAGE	0.6521 [0.6070, 0.6982]	1.342e-02	0.0948	0.0622
Transolver	0.6979 [0.6467, 0.7510]	1.677e-02	0.1033	0.0673
Galerkin Transformer	0.8150 [0.7536, 0.8769]	2.332e-02	0.1206	0.0786
PointNet	0.8899 [0.8257, 0.9593]	2.291e-02	0.1260	0.0880
Voxel				
U-Net	0.7050 [0.6306, 0.7753]	1.482e-02	0.0981	0.0578
U-FNO	0.7568 [0.6709, 0.8478]	1.653e-02	0.1037	0.0602
FNO	0.8387 [0.7798, 0.8952]	1.915e-02	0.1167	0.0728
U-NO	0.8303 [0.7591, 0.9089]	1.899e-02	0.1142	0.0696
F-FNO	1.0005 [0.9462, 1.0601]	2.787e-02	0.1397	0.0872

(b) Magnitude, direction, and explained variance

Model	Mean $\lvert\mathbf{u}\rvert$ MAE	Angle (°)	Cosine	Mean case R^2
Unstructured				
GraphSAGE	0.0788	48.26	0.5629	0.5189
Transolver	0.0901	52.78	0.4902	0.4354
Galerkin Transformer	0.1008	60.91	0.3837	0.2270
PointNet	0.1177	62.09	0.3830	0.0764
Voxel				
U-Net	0.0796	52.21	0.4674	0.3602
U-FNO	0.0805	52.88	0.4654	0.2236
FNO	0.1009	66.15	0.3070	0.1936
U-NO	0.0945	61.56	0.3624	0.1593
F-FNO	0.1197	75.73	0.1925	-0.1169

Table 36: R3 steady stored-gauge pressure diagnostics on the same 79 held-out sources. MSE is in Pa^2; RMSE and MAE are in Pa. Columns average per-condition metrics within sources, then across sources. Per-case R^2 values are averaged without clipping; negative per-case values indicate greater squared error than prediction of that case's target mean.

Model	RelL2 95% CI	Mean MSE (Pa^2)	Mean RMSE (Pa)	Mean MAE (Pa)	Mean case R^2
Unstructured					
GraphSAGE	0.5525 [0.4679, 0.6570]	2.938e+04	96.151	75.164	-0.9774
Transolver	0.5783 [0.5083, 0.6681]	3.697e+04	107.712	85.817	-1.0354
Galerkin Transformer	0.6667 [0.5741, 0.7917]	4.912e+04	122.183	97.056	-1.8980
PointNet	0.7718 [0.6782, 0.8885]	4.202e+04	130.467	104.165	-2.6911
Voxel					
U-Net	0.7930 [0.6700, 0.9208]	4.344e+04	125.318	99.013	-2.6535
U-FNO	0.7925 [0.6849, 0.9198]	4.833e+04	130.274	102.988	-2.6587
FNO	0.9126 [0.7668, 1.0761]	4.305e+04	130.897	105.238	-3.8250
U-NO	0.8946 [0.7478, 1.0627]	4.303e+04	129.908	104.490	-3.8761
F-FNO	1.1466 [0.9527, 1.3685]	6.332e+04	155.237	126.218	-7.0027

Table 37: R3 reset-window $4 \to 4$ WSS diagnostics on 79 held-out source geometries, with observed histories restored between windows. Values are source means of per-window metrics. MSE is in Pa^2; RMSE, component MAE, and magnitude MAE are in Pa. Direction metrics include only locations at which both vector magnitudes exceed 10^{-8} Pa.

(a) Field errors

Model	RelL2 95% CI	Mean MSE	Mean RMSE	Mean MAE
Unstructured				
Transolver	0.1084 [0.0969, 0.1218]	9.021e+01	3.694	2.075
Galerkin Transformer	0.1090 [0.0977, 0.1221]	9.595e+01	3.747	2.091
PointNet	0.1484 [0.1373, 0.1610]	1.332e+02	4.582	2.648
GraphSAGE	0.2235 [0.2014, 0.2498]	1.633e+02	5.577	3.240
Voxel				
U-Net	0.2064 [0.1958, 0.2191]	2.019e+02	5.919	3.392
F-FNO	0.2104 [0.2002, 0.2225]	2.153e+02	6.037	3.445
FNO	0.2145 [0.2044, 0.2263]	2.275e+02	6.194	3.504
U-FNO	0.2227 [0.2123, 0.2346]	2.335e+02	6.437	3.678
U-NO	0.2230 [0.2122, 0.2354]	2.419e+02	6.491	3.699

(b) Magnitude and direction

Model	Mean magnitude MAE	Angle (°)	Cosine
Unstructured			
Transolver	2.849	7.78	0.9558
Galerkin Transformer	2.878	7.83	0.9556
PointNet	3.983	9.15	0.9464
GraphSAGE	4.914	14.46	0.9144
Voxel			
U-Net	5.816	9.01	0.9457
F-FNO	5.918	9.42	0.9436
FNO	6.042	9.09	0.9459
U-FNO	6.405	8.84	0.9479
U-NO	6.437	9.25	0.9450

I RELEASE ARTIFACTS, DATA ACCESS, AND REPRODUCTION

Review packages and supported tasks. The inspection subset contains four training sources and eight descendants, with all eight steady conditions and full transient fields. Selection spans quantiles of transient HDF5 file size, first among eligible training sources and then among descendants within each selected family.

Native-resolution wall coordinates and 100-frame WSS arrays for 277 training and 42 validation sources support source-only WSS training and feedback adaptation with the supplied recipes and normalization statistics. The fixed-test package provides 4,096 wall points and 100 WSS frames for each of the 79 test sources, the R1/R3 Transolver weights, and six matched $F = 16$ adaptation checkpoints. Its script recomputes reset, rollout, and cycle metrics.

The supplementary code ZIP includes training and evaluation scripts, splits, availability records, normalization statistics, and source-level results for reproducing reported aggregates. A compact HDF5 sample exercises the loaders. The Figshare review collection hosts the data and checkpoint ZIPs.

GraphSAGE allocation retraining requires each pool's selected descendants, common source fine-tuning fields, and validation and test fields under all eight steady inlet conditions. These data are provided in the full release. The full VTU/VTK and HDF5 corpus will receive permanent hosting after de-anonymization, with upstream notices. Complete OpenFOAM case configurations are archived separately.

Reproduction scope and attribution. Release versions identify the source split and preprocessing used for each result. The data documentation specifies physical units and time grids. Code uses Apache-2.0, and AneuX-derived data carry CC BY-NC 4.0 terms. The upstream notices specify AFBench's CC BY-NC-SA 4.0 data license (Liu et al., 2024), the airfoil geometry archive, and the XFoil version and source revision used to recompute pressure coefficients.

Table 38: Reproduction tasks supported by the anonymous review packages and the full release. For numerical provenance, "Spec." denotes the solver specification; "Archive" denotes retained OpenFOAM case configurations.

Reproduction task	Materials and use	Review	Full
Cohort and schema	Source-family splits, availability records, and the compact HDF5 sample; verifies identifiers, inherited splits, array shapes, units, and time grids.	✓	✓
Metric and report	Source-level result JSON files and evaluators; regenerates reported aggregates, paired intervals, tables, and figures.	✓	✓
Loader and evaluator example	Baseline configurations, loaders, and the compact sample; exercises data loading and endpoint computation on sample fields.	✓	✓
Checkpoint inference	Fixed 79-source WSS samples and actual Transolver weights; recomputes reset, rollout, and cycle metrics.	✓	✓
Source-only WSS training and adaptation	Native-resolution WSS arrays for 277 training and 42 validation sources, with training recipes and normalization statistics.	✓	✓
Steady allocation retraining	Pool manifests, selected descendant fields, common source fine-tuning fields, and complete steady validation and test fields.	–	✓
Full retraining	Complete VTU/VTK and HDF5 corpus with training recipes; recreates selected checkpoints and source-level records.	–	✓
Numerical provenance	Solver assumptions in this appendix and retained OpenFOAM case configurations; documents upstream field generation.	Spec.	Archive